Article:

Lyu, Y., Li, A. orcid.org/0000-0001-8897-0447, Wu, J. et al. (4 more authors) (2025) Enhanced mechanical performance of 3D printed continuous carbon fibre reinforced polyphenylene sulphide composites through dopamine treatment and post-processing compression. Composites Part A: Applied Science and Manufacturing, 190. 108627. ISSN 1359-835X

https://doi.org/10.1016/j.compositesa.2024.108627

Composites: Part A 190 (2025) 108627

Contents lists available at ScienceDirect

Composites Part A

journal homepage: www.elsevier.com/locate/compositesa

Enhanced mechanical performance of 3D printed continuous carbon fibre reinforced polyphenylene sulphide composites through dopamine treatment and post-processing compression

Yahui Lyu [a], Aonan Li [a], Jiang Wu [a], Vasileios Koutsos [a], Chun Wang [b], Conchúr M.Ó. Brádaigh [c], Dongmin Yang [a,*]

[a] School of Engineering, Institute for Materials and Processes, University of Edinburgh, EH9 3FB, Edinburgh, UK
[b] Institute of Functional Surfaces, School of Mechanical Engineering, University of Leeds, LS2 9JT, Leeds, UK
[c] Department of Mechanical Engineering, University of Sheffield, S10 2TN, Sheffield, UK

ARTICLE INFO

Keywords:
Continuous carbon fibre reinforced thermoplastic composites
Additive manufacturing
Polydopamine
Post-processing
Interlaminar properties

ABSTRACT

This study investigates the impact of dopamine-treated carbon fibre reinforcement and post-processing techniques in polyphenylene sulphide (PPS) composites, with a focus on improving interfacial and interlayer properties. The synergistic effects of continuous carbon fibre (CCF) treatment with polydopamine/silica nanoparticles (PDA/NPs) and post-processing on the mechanical performance of 3D printed composites are explored. The findings demonstrate that treated composites exhibit significant improvements in interlaminar properties, with increases in flexural strength by 27% and interlaminar shear strength (ILSS) by 172%, compared to untreated specimens. Molecular dynamics (MD) simulations and nano-indentation tests reveal the mechanisms behind the improved fibre/matrix interfacial adhesion attributing to PDA/NPs network on the fibre. Differential scanning calorimetry (DSC) and microscopic analyses are utilised to assess enhancements in crystallinity, void content, and fibre orientation after post-processing. Furthermore, we introduce a novel post-processing method involving a salt bath, which aligns with the unique advantages offered by 3D-printed complex composites. This approach is validated with two complex demonstrative geometries, confirming its effectiveness in maintaining structural integrity while enhancing interlayer properties. The integration of pre-processing with the PDA/NPs network and post-processing techniques with a salt bath offers particular benefits for additively manufactured high-performance materials.

1. Introduction

Continuous carbon fibre reinforced thermoplastics (CCFRTP) have emerged as a cornerstone in modern aerospace and automotive industries, mostly attributed to their unique combination of light weight, superior strength, high modulus and improved recycling feasibility [1]. These CCFRTP composites are increasingly replacing traditional metal materials, leading to advancements in fuel efficiency and structural integrity in various applications. The incorporation of continuous fibres in polymer composites is a notable advancement over short fibre reinforcements [2–4]. Continuous fibres provide a substantial enhancement to the mechanical properties of composites, including tensile strength and durability. However, the difficulty in impregnating fibres due to the high viscosity of the polymer in the molten state still limits the application of CCFRTP [5]. The manufacturing of CCFRTP involves impregnation processes like film stacking method, commingle fabrics, and dry powder impregnation method [6,7]. Each of these methods comes with its own set of limitations while effective in certain applications. Film stacking method is effective for producing semi-finished products, offering a relatively easier way to manufacture. However, it often involves the limitation of material selection and high initial setup costs [8]. Commingle fabrics allow for the creation of higher strain and impact parts and are relatively low cost. The main drawback is the requirement of precise control, particularly for complex geometries [9]. Dry powder impregnation process is ideal for processing the high-viscosity polymers and is free of evaporated chemical agents [10]. The impregnated fibre tows can be used directly in manufacturing the final products, which reduce the costs of secondary material processing. It

---

* Corresponding author.
E-mail address: Dongmin.Yang@ed.ac.uk (D. Yang).

https://doi.org/10.1016/j.compositesa.2024.108627
Received 4 April 2024; Received in revised form 23 October 2024; Accepted 28 November 2024

also offers an effective approach to produce the filaments for manufacturing products with complex geometries.

In recent years, additive manufacturing (AM) or 3D printing, has been gaining momentum in manufacturing fibre-reinforced polymer composites [11–13]. This technology stands out for its ability to fabricate components with complex geometry that were previously challenging or impossible to create using conventional methods. Moreover, AM offers remarkable control over fibre orientation, streamlined manufacturing processes, and significant cost reductions, especially in low-volume or custom production runs [14–17]. Among the various AM techniques, material extrusion (MEX) is the most widespread technology due to its versatility in creating thermoplastic composites [18–21]. This method is particularly adept at working with both discontinuous or continuous reinforcements, making it a versatile option for a wide range of applications.

However, the full potential of 3D printing of CCFRTP is yet to be achieved, primarily due to challenges in impregnation during pre-processing, and consolidation during post-processing [22]. Commonly used commercial carbon fibre tows often struggle to bond effectively with thermoplastic matrices. The poor interfacial adhesion leads to heightened risks of fracture at the interface under loading, which is the critical vulnerability in the composites structure [23–25]. Additionally, the inherent principle of MEX, involving the extrusion of materials at high temperature followed by rapid cooling and solidification upon contact with cooler surfaces, present additional challenges [26–28]. The rapid temperature change can lead to weak adhesion between successive layers and increased porosity within the composites, adversely affecting its overall integrity and performance. Although the mechanical properties along the printing direction may be comparable with those produced by traditional manufacturing methods, the response of these materials under transverse or interlaminar loads is significantly compromised due to the inherent defects of weak adhesion on the fibre/matrix interface and insufficient thermal consolidation of the layers during the layer deposition process [29,30].

In response to these limitations, this work introduces an innovative approach that involves treating the commercial carbon fibre with silica nanoparticles and polydopamine hybrid network [31]. This treatment aims to enhance fibre/matrix adhesion significantly. We then use this treated fibre to fabricate continuous carbon fibre reinforced polyphenylene sulphide (CCF/PPS) filament, designed for optimised performance in 3D printing application. Additionally, we propose a post-processing method that applies high temperature and pressure to mitigate layer adhesion defects. The mechanical performance under flexural loads and interlaminar shear loads are measured to investigate the synergistic effect of pre-processing and post-processing. The improvement mechanisms are thoroughly investigated using a multifaceted approach. For the pre-processing, we employ molecular dynamic (MD) simulation and single fibre push-out test to elucidate the underlying mechanisms contributing to the enhanced interfacial adhesion. For the post-processing, we analyse the microstructure and crystallinity to gain insights into the structural evolution. Further, X-ray computed tomography (XCT) scanning is utilised to explore the synergetic effects of combined pre-treatment and post-processing methods on improving the interlaminar performance, particularly under short beam bending conditions. These comprehensive analyses help in understanding the interfacial and interlayer properties of the composite materials and guides the optimisation of our processes. Ultimately, we propose and validate an optimised post-processing method involving a salt bath. This method demonstrates its feasibility to process the complex 3D printed structures, including two-dimensional lightweight perforated designs and intricate three-dimensional integrated structures.

2. Experimental setup

2.1. Materials

Continuous carbon fibre tow (3K) was procured from Easy Composites Ltd, Stoke on Trent, United Kingdom. Tetraethoxysilane (TEOS), dopamine hydrochloride (DP) and tris (hydroxymethyl)-aminomethane (Tris) were sourced from Merck Life Sciences Ltd, United Kingdom. Polyphenylene sulphide (PPS, Torelina A900) was produced by Toray Industries, Japan. Acetone, employed in the desizing process, was acquired from Fisher Scientific Ltd, Leicestershire, United Kingdom. All chemicals were utilised as received, except reported otherwise.

2.2. Modification of continuous carbon fibre

The process of modifying the continuous carbon fibre tow began with the synthesis of colloidal silica nanoparticles (NPs), employing tetraethoxysilane (TEOS) as the precursor [32]. The initial step involved the desizing of the as-received carbon fibre tow using acetone. Following this, we prepared a reaction medium by dispersing the silica nanoparticles (Fig. 1(a)) in a 0.1% Tris-buffered solution (pH 8.5), an environment conducive to dopamine's self-polymerisation. The next stage of the process involved the simultaneous introduction of the carbon fibre and dopamine hydrochloride into this buffered nanoparticle solution. This step was conducted at ambient room temperature, using an ultrasonic device to facilitate the uniform coating of the carbon fibre with the PDA/NPs hybrid network (refer to Fig.1(b)). The carbon fibre tow was then left immersed in this modification solution for a duration of 16 hours, ensuring thorough treatment. Post-immersion, the carbon fibre tow underwent a rinsing process, being washed three times with ultrapure water to remove any unreacted components or residues. The final step in the pre-treatment process was the drying of the carbon fibre tow. This was achieved by placing it in an oven and maintaining a consistent temperature of 60 °C for a prolonged period of 48 hours, resulting in the acquisition of the modified, pre-treated continuous carbon fibre.

2.3. Filament fabrication of CCF/PPS composites

Continuous carbon fibre reinforced PPS composites were fabricated using a house developed filament-line, modified from our previous work [33]. The equipment is shown in Fig. S1. Initially, the continuous carbon fibre tow was held under tension using a wind-up spooler. This setup was critical for ensuring uniform fibre alignment and tension during the subsequent impregnation process. For the formation of pristine continuous carbon fibre reinforced PPS composites (p-CCF/PPS), PPS powder was evenly distributed onto the surface of the carbon fibre. The coated fibres were then passed through a nozzle, where the powder was melted at high temperatures to create a resin bath. The pultrusion temperature was precisely controlled and set at 320°C to facilitate optimal melting and impregnation. As the carbon fibre tow was drawn through this resin bath, it became thoroughly impregnated with the PPS resin, forming the p-CCF/PPS. For the production of the treated composites (t-CCF/PPS), dry continuous carbon fibre was first subjected to a treatment involving a modification solution containing polydopamine and silica nanoparticles. This pre-treatment involved immersing the carbon fibre in the solution, followed by a thorough rinsing and drying process. Once prepared, the treated carbon fibres were compounded with PPS powder through the filament-line following the same process as above. This step was crucial for ensuring the even distribution and integration of the PPS powder with the modified carbon fibre, resulting in the formation of the t-CCF/PPS composites.

2.4. 3D printing and post-processing of CCF/PPS composites

The fabrication process progressed to the 3D printing stage, where

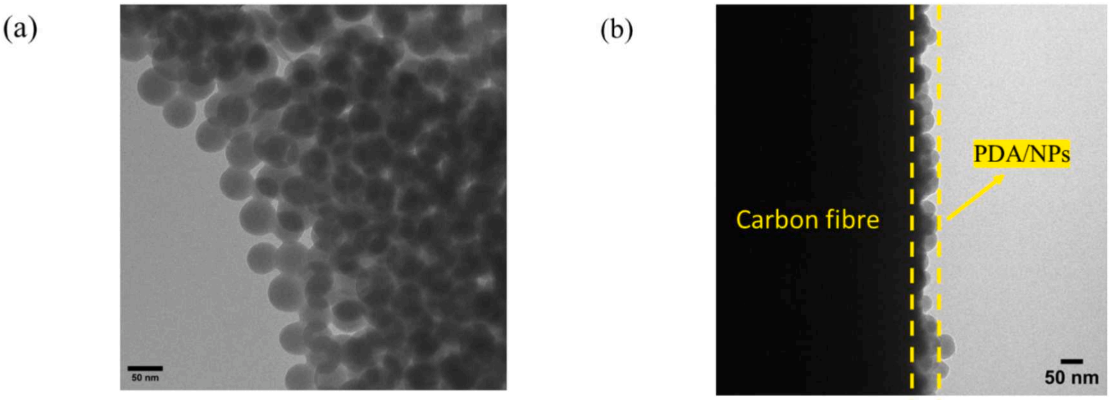

Fig. 1. (a) TEM images of synthesised silica nanoparticles; (b) TEM images of PDA/NPs layer on the surface of carbon fibre.

both types of the previously fabricated continuous filaments were utilised. A circular-similar cross-section, possessing a diameter of approximately 600 μm, was observed for the 3K continuous carbon fibre/polyphenylene sulphide (CCF/PPS) filament, featuring an average fibre volume fraction of around 50% (refer to Fig. 2(a)). A high-temperature 3D printer (Creatbot F430) was employed to manufacture CCF/PPS composites from these filaments. For this purpose, a specific fibre placement nozzle with a diameter of 1.3 mm, sourced from Markforged Ltd., United States, was integrated into the 3D printer (see Fig. 2(b)). This setup allowed for the precise and controlled deposition of the continuous filament during the printing process. The SEM images of a printed single strip is shown in Fig. 2(c). Table S1 presents the printing parameters for the CCF/PPS filament.

As shown in Fig. 2(a) and (c), the fibre distribution is not very uniform due to insufficient impregnation in the produced CCF/PPS filament. After applying moderate pressure with the printer nozzle, impregnation improves but the fibre distribution in the printed strip remains somewhat uneven. Therefore, it is essential to apply compression pressure on the as-printed parts to ensure more uniform fibre distribution and consistent material performance.

Following the 3D printing, the composites underwent a critical post-processing phase, which was conducted using a Pinette Emidecau Industries (P.E.I.) hot-press machine. The hot-press program is depicted in Fig. S2(a) and the images of as-printed and post-processed specimens are also presented in Fig. S2(b). This stage was implemented through two distinct hot-press methods: mould-based and salt bath-based. In the mould-based post-processing method, the printed composites were placed within a specially designed mould (refer to Fig. 2(d-1)). They were then subjected to hot-press under elevated temperatures and high pressure. Alternatively, in the salt bath-based hot press method, the printed composites with complex geometries were initially immersed in a salt bath prior to being hot-pressed (refer to Fig. 2(d-2)). The cuboid mould was filled with ground salt, and the printed object was submerged in the salt. This process enables the salt to act as a support to maintain the detailed features and evenly distribute the pressure in all directions during the hot-pressing procedure. The unique property of the salt, remaining un-melted under high temperatures and pressures, was a crucial aspect of this method. This approach allowed for the successful post-processing of complex two-dimensional and intricate three-dimensional structures, including those with holes and detailed geometries. The salt bath method was particularly effective in reducing void content in the final composites through thickness while maintaining precise dimensions in other directions.

2.5. *Mechanical test of 3D printed CCF/PPS composites*

The mechanical properties of 3D printed CCF/PPS composites were evaluated using a three-point bending test. This test was conducted in accordance with the ASTM D7264 standard. For this purpose, an Instron 3369 test machine equipped with a 50 kN load cell was utilised. The test specimens were rectangular, each with dimensions of 80 mm in length, 13 mm in width, and 4 mm in thickness. During the testing, a consistent crosshead displacement rate of 1.0 mm/min was maintained to ensure uniform application of stress. To account for variability and ensure statistical reliability, each test group comprised three specimens.

The assessment of interlayer properties was carried out by measuring the interlaminar shear strength (ILSS). This measurement followed the ASTM D2344 standard, utilising the short beam test method. Test samples were prepared from printed CCF/PPS composite laminates, each sample having dimensions of 24 mm in length, 8 mm in width, and 4 mm in thickness. The ILSS test was performed using an Instron 3369 universal testing machine with a load cell of 10 kN. A key parameter in this test is the span length, which was precisely set to 16 mm. Throughout the test process, the rate of the crosshead was consistently maintained at 1.0 mm/min. To ensure comprehensive and accurate assessment, each composite laminate type was subjected to three repeated tests.

2.6. *Nanoindentation tests*

Nanoindentation tests were performed using the NanoTest Vantage system (Micro material) to conduct single fibre push-out tests, as referenced in [34].To prepare the push-out samples, slices of dimensions 13 mm × 4 mm × 2 mm were cut out from 3D printed unidirectional (UD) composite specimens. These slices were then vertically embedded in a polymethyl methacrylate (PMMA) tube filled with liquid epoxy resin. After curing, the epoxy cylinder was ground and polished by a polisher (ATA Saphir 520). This process involved the use of SiC abrasive paper, with grain sizes escalating from 180, 400, 800, 1200 and 2000, ensuring a gradual and uniform abrasion. Subsequently, finer polishing was achieved using the diamond powder with grain size of 3 μm and 1 μm. To ensure uniformity and perpendicularity to the polishing plane, the cylinder was secured in an adapter during this procedure. After completing one side, the specimen was flipped, and the opposing side was similarly ground and polished until the composite slice reached an approximate thickness of 100 μm (as shown in Fig. 3(a)). Specimens were positioned on a fine mesh featuring a 26 μm diameter groove, ensuring precise alignment during test. The micrographs of composites on the front side and mesh on the back side are shown in Fig. 3(a-1) and (a-2), respectively.

Fig. 3(b) illustrates the schematic of nanoindentation loading and unloading. Testing parameters included a loading rate set at 20 nm/s, utilising a triangular diamond pyramidal indenter (Berkovich tip) to exert force on the fibres. A series of push-out tests were unloaded at 100 nm/s in the unloading steps. Randomly selected fibres embedded within the PPS matrix were subjected to a maximum load of 100 mN.

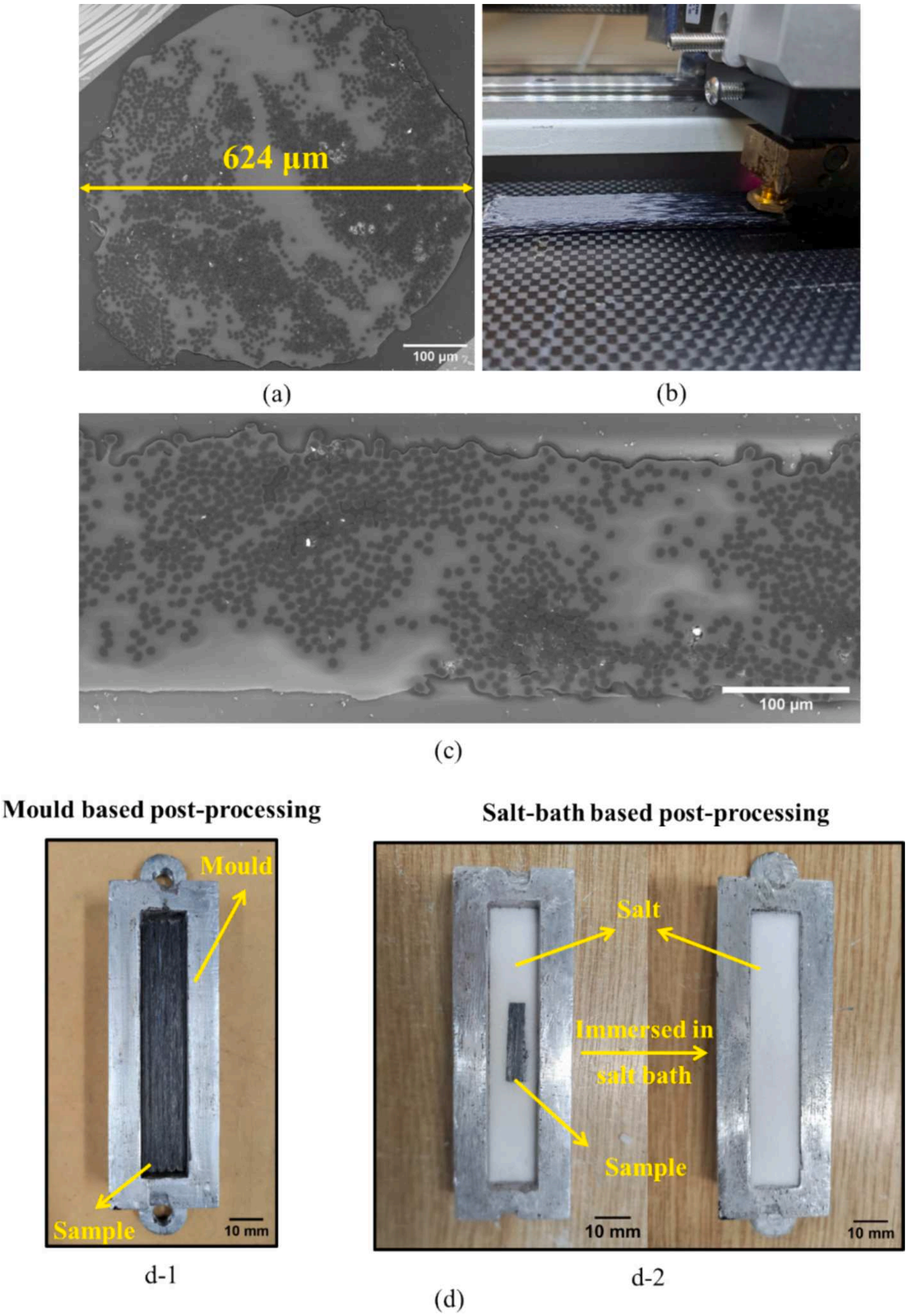

Fig. 2. (a) Cross-section of produced 3K CCF/PPS filament; (b) printing process of CCF/PPS filament; (c) printed single strip; (d) samples in mould-based post-processing for three-point bending (d-1) salt-bath based post-processing for short-beam bending (d-2).

Subsequently, the cross-sectional areas of these tested samples were examined using scanning electron microscopy (SEM) to assess the interfacial interactions. The representative indentation pit is shown in Fig. 3(c).

The IFSS is calculated based on the Eq. (1).

$$\tau_{IFSS} = \frac{F_{max}}{2\pi r_c l_s} \tag{1}$$

where F_{max} represents the maximum load at which debonding between fibre and matrix occurs, usually identifiable as the initial peak load in the test data [35]; r_c is the radius of carbon fibre (3.5 µm for T700); and l_s is the sample thickness.

2.7. Thermal properties of 3D printed recycled composites

Dynamic Mechanical Analysis (DMA) was employed to characterise the viscoelastic properties of 3D printed CCF/PPS composites, involving the application of sinusoidal oscillating stress to the sample. For this study, a TA Instruments Discovery DMA 850 apparatus was utilised. The specimens prepared for testing measured 55 mm in length, 13 mm in width, and 2 mm in thickness. The DMA tests encompassed a temperature sweep ranging from 35 °C to 250 °C, with a controlled ramp rate of 2 °C/min. This procedure was conducted in the dual cantilever mode to optimally evaluate the behaviour under bending stresses. A frequency of 1 Hz was set for the tests, coupled with an amplitude of 30 µm, to effectively measure the response to stress over time. Additionally, all tests were conducted in a nitrogen atmosphere to prevent any

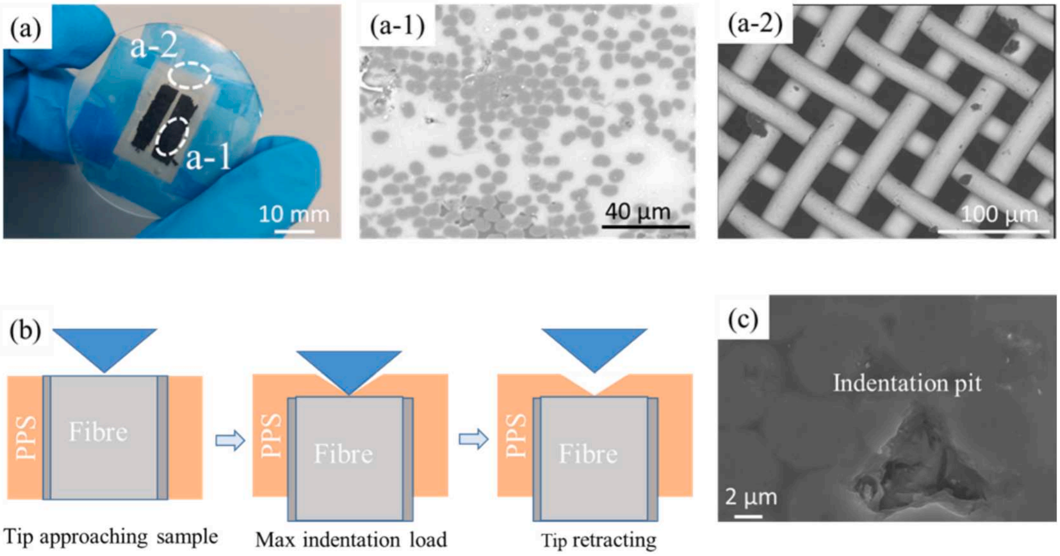

Fig. 3. (a) Image of the prepared nanoindentation sample: (a-1) micrograph of composites on the front side (a-2) micrograph of mesh on the back side; (b) schematic of nanoindentation loading and unloading; (c) indentation pit after tip retraction.

degradation of the samples due to environmental factors, ensuring the accuracy and reliability of the test results.

The thermal behaviour of the composites was analysed using Differential Scanning Calorimetry (DSC), employing a PerkinElmer DSC 8000 instrument. During the testing procedure, the samples underwent a controlled temperature program. This program involved an initial heating phase from 30 °C to 300 °C at a rate of 20 °C/min, followed by a cooling phase back down to 30 °C. Subsequently, a second heating cycle mirrored the first, maintaining the same temperature ramp rate. Throughout both heating cycles, heat flow was precisely measured for each sample, which were placed in alumina crucibles. Total enthalpy of the melting process as indicated in the DSC curve was calculated automatically using Pyris software. This data was critical in determining the crystallinity (X_c) of the printed composites, calculated using the following Eq. (2):

$$X_c(\%) = \frac{\Delta H_m}{\Delta H_f(1-x)} \times 100\% \tag{2}$$

where ΔH_m represents the observed melting enthalpy, ΔH_f signifies the enthalpy of fusion of 100% crystalline PPS, which is 80 J/g and x represents the weight fraction of carbon fibre. The measurements are derived from the first heating run of the heat flow [36].

2.8. Microstructure characterisation and morphology analysis

Samples were first sectioned to appropriate dimensions and polished to reveal clear cross-sectional areas necessary for accurate imaging. The microstructure of both raw filament and printed composites was observed using a SEM (HITACHI TM4000Plus), and high-quality micrographs were captured of the composite cross-sections. The images were then quantitatively analysed using ImageJ software, which allowed for the differentiation between fibre and matrix based on contrast differences. The total area occupied by the fibres and the matrix was measured from the segmented images. The volume fraction of fibres was then calculated using the Eq. (3):

$$V_f(\%) = \frac{V_{fibre}}{V_{fibre} + V_{matrix +} V_{void}} \times 100\% \tag{3}$$

where V_f is the volume fraction of the fibres, V_{fibre}, V_{matrix} and V_{void} are the total volume occupied by the fibres, matrix and void content, respectively.

To ensure accuracy, measurements were taken from multiple images across different sample sections and averaged.

Additionally, the surface morphology of carbon fibres was examined using transmission electron microscopy (TEM, JEOL, JEM1400 Plus). This technique offered a more in-depth view of the fibres at a molecular level, contributing significantly to our understanding of the composite structure.

The failure mechanisms of the specimens from the short beam tests were investigated using the in-house developed X-ray computed tomography (XCT) facility at the University of Edinburgh. XCT scans were performed at an accelerating voltage of 70 kV and a power of 24 W. To ensure the acquisition of high-quality images, both in terms of contrast and intensity, the exposure time was set to 2 seconds. The raw scan data were then processed and visualised in 3D using the commercial software Avizo. This software's volume rendering and slicing capabilities were particularly used in identifying failure modes at various locations within the specimens. The application of XCT imaging allowed for a capture of the failure modes induced by shear loading within the specimens.

3. Molecular dynamics simulation

The interactions between the carbon fibre, PDA/NPs network and the PPS matrix at the atom or molecular level were investigated using molecular dynamic (MD) simulations. These simulations were carried out using the Materials Studio software, employing the Forcite module. The basis for all simulations was the COMPASS (condensed phase optimised molecular potential for atomistic simulation studies) force field. This comprehensive force field encompasses valence energy, including both diagonal terms and cross terms, as well as non-bond energy. The diagonal terms cover aspects such as bond, angle, torsion, and inversion, whereas the cross terms include stretch-stretch, stretch-bend-stretch, stretch-torsion-stretch, separated-stretch-stretch, torsion-stretch, bend-bend, torsion-bend-bend, and bend-torsion-bend interactions. The non-bond energy component accounts for van der Waals and electrostatic interactions [37].

3.1. Modelling of hybrid layers on CF surface

At the nano-scale, the carbon fibre (CF) surface is characterised by a highly graphitic arrangement comprising sp2 carbon atoms. The atomic-scale features of the CF surface, however, remain less defined. For the purpose of these simulations, carbon fibre models were constructed based on graphene or graphite crystals, representing an idealised and unsized CF surface, as commonly used in literature [38]. Despite the simplified nature of this graphite carbon fibre surface model, its use in simulations of graphite-polymer composites interfaces, in conjunction with experimental work, is useful in elucidating the molecular-level mechanics of the carbon fibre-matrix interface [39–42]. In this model, four layers of graphite with a density of 1.78 g/cm^3 and an interlayer spacing of 3.4 Å were constructed in a periodic simulation cell.

It is widely accepted that the formation of polydopamine (PDA) molecules stems from the oxidation of dopamine (DPA), along with intramolecular cyclisation and the redistribution of electrons, with oxidation induced by air being crucial to this self-polymerisation process. Besides the reactions that involve the formation of covalent bonds, the non-covalent self-assembly process also plays a significant role in the synthesis of PDA [43]. Research indicates that the final structure of PDA predominantly comprises oligomers, which are connected through dihydroxy-indole and indole-quinone units via benzene ring linkages [44]. In our simulation system, PDA was therefore considered as a polymer-like aggregate composed of oligomer units connected through tetramer linkages [45].

Three models representing interactions between CF and SiO_2, CF and PDA, and PDA and SiO_2, respectively, were built to study the adsorption energies and evaluate the interfacial strength. The geometry of each interface structure was first optimised using the NVT ensemble at 298 K, followed by equilibrium achieved through annealing simulations ranging from 300K to 500K over five cycles. The final frames are presented in Fig. S3 (a-c). Additionally, a multilayer model containing CF, PDA, and SiO_2 was created to investigate the microscopic distribution

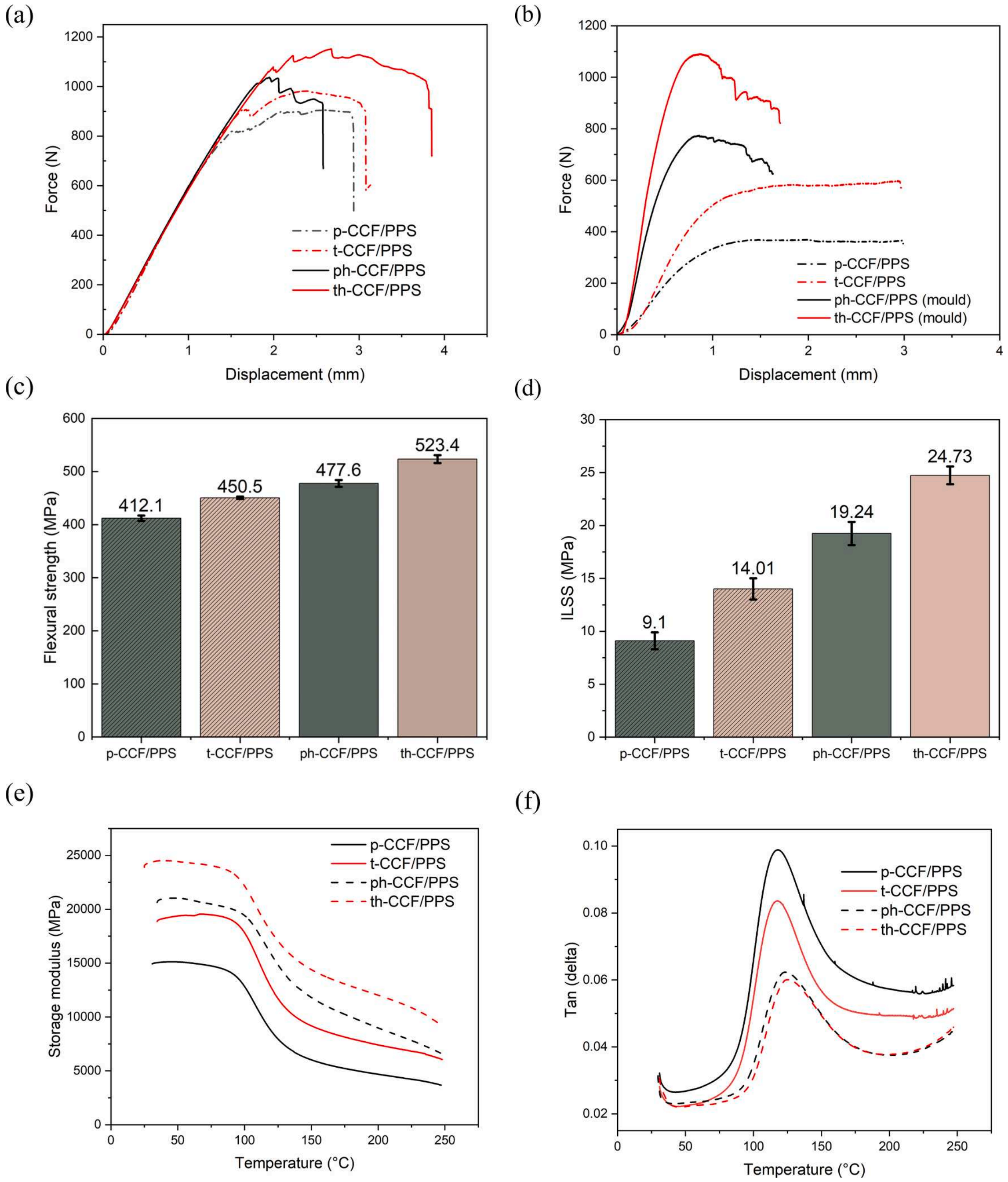

Fig. 4. (a) force-displacement curve of three-point bending test; (b) force-displacement curve short beam bending test; (c) flexural strength values and (d) ILSS values; (e) storge modulus and (f) damping factor of p-CCF/PPS, t-CCF/PPS, ph-CCF/PPS and th-CCF/PPS.

and geometry configuration of the PDA/NPs hybrid networks on the carbon fibre surface, as shown in Fig. S3(d). The models underwent equilibration using the aforementioned method, with results presented in Fig. S3(e).

3.2. *Single fibre push-out simulation*

In order to build a model with similar conditions as experiments, a PPS polymer model was constructed from an amorphous cell mixed with its monomers at an initial density of 1.3 g/cm^3. This model was designed with periodic boundary conditions (PBC). The PPS polymer matrix layer structures were then established and sufficiently equilibrated to simulate the shear behaviour of the single carbon fibre. The mechanical response at the interface was assessed using push-out MD simulations [40,46]. Here, the CF substrate was pushed out of the polymer matrix, and the change in total system potential energy was monitored. The CF substrate was configurated as an independent rigid body, and laterally pulled out along the x-direction at a constant velocity of 2.5 Å/ps using the NVT ensemble at 298K over 18 ps. The variation in potential energy is determined by the change in interfacial interaction force between carbon fibre and the PDA/NPs layer, and PDA/NPs layer and PPS polymer. Therefore, we have minimised the thickness of in-depth carbon fibre layer to control the system size and accelerate the computation time [47,48]. The Cartesian position of 50% in-depth atoms of PPS polymer in the cell was fixed to simulate real experimental conditions accurately. Free motion of other atoms in the cell was maintained during the CF push-out simulation. The maximum displacement of the substrate was 45 Å, offering valuable insights into the interfacial dynamics and molecular interactions under simulated shear conditions.

4. Results and discussion

4.1. *Mechanical performance with improved interlaminar properties*

To assess the impact of the PDA/NPs hybrid networks and post-processing techniques on the macro-mechanical properties of the composites, we analysed the force-displacements curves and ultimate flexural strength under the three-point bending load (Fig. 4(a) and (c)). This analysis included unidirectional coupons of printed composites with pristine carbon fibre (p-CCF/PPS), printed composites with treated carbon fibres (t-CCF/PPS), as well as their hot-pressed counterparts using mould-based post-processing method (as shown in Fig. 2(d-1)), *i.e.*, ph-CCF/PPS and th-CCF/PPS. The experimental results revealed notable enhancements in flexural strength following treatments. Specifically, composites exhibited an increase of 9.3% in flexural strength with the sole application of the PDA/NPs treatment and an increase of 15.9% with only post-processing treatment (using a specially designed mould). Notably, the parts that underwent post-processing with treated carbon fibre showcased the highest flexural strength, which was 27.0% greater than that of p-CCF/PPS. These findings indicate that the combination of PDA/NPs treatment and post-processing significantly enhanced the mechanical response of CCF/PPS composites, evidencing the efficacy of this two-step treatment approach in enhancing interfacial properties.

Further examination of the interlaminar properties was conducted through the measurement of interlaminar shear strength (ILSS) under a short-beam three-point bending load for the aforementioned four types of composites, as detailed in Fig. 4(b) and (d). Starting with the untreated coupons featuring pristine carbon fibre (p-CCF/PPS), the ILSS was found to be 9.1 MPa, setting a baseline for the subsequent treatments. When carbon fibres were treated with PDA/NPs, the ILSS values increased significantly by 52.2%, attributing to the effectiveness of the nanoparticle treatment in enhancing the fibre-matrix interface. The impact of post-processing was even more obvious, with ILSS values effectively doubling, indicating a substantial reinforcement of the interlayer bonds within the composite. This marked ILSS value of 24.73 MPa for composites that underwent both carbon fibre surface treatment and interlayer consolidation.

The DMA curves depicted in Fig. 4(e) and (f) provide a comprehensive overview of the thermal-mechanical performance of the various composite configurations across a temperature spectrum from room temperature to 250 °C. The storage modulus, representing the elastic response of the material, typically decreases with an increase in temperature due to the softening of the polymer matrix. This trend is consistent across all composite types, as observed in Fig. 4(e).

For the p-CCF/PPS composites, the modulus begins at a substantial value but experiences a marked decrease as the material transitions through its glass transition region. The t-CCF/PPS composites display an obvious increase in the storage modulus at lower temperatures, as a result of the positive impact of the PDA/NPs treatment on the stiffness of the composite. This improvement, quantified at 25.9% at 35 °C, indicating the effectiveness of surface treatment in reinforcing the composite's elastic properties. Upon examining the effects of post-processing, hot-pressed ph-CCF/PPS and th-CCF/PPS composites demonstrate a less drop in the storage modulus with increasing temperature, signifying superior performance and stability. In particular, the th-CCF/PPS composites achieve an impressive storage modulus of 24.5 GPa at 35 °C and 9.2 GPa at 250 °C, which is a remarkable 62.7% and 149.4% increment compared to the untreated samples.

It becomes evident that this treatment plays a vital role in enhancing the thermal stability of the composites. The Fig. 4(f) illustrates the tan delta (damping factor) curves, which offer insight into the material's damping characteristics and glass transition temperature (T_g). The p-CCF/PPS composites have a T_g of 117 °C, while the th-CCF/PPS composites exhibit an increased T_g of 127 °C. This elevation in T_g for the th-CCF/PPS composites can be attributed to the enhanced fibre/matrix adhesion and the stabilisation of the polymer chains achieved through the synergistic effects of PDA/NPs treatment and post-processing. The shift in T_g also suggests changes in the semi-crystalline structure of the polymer, indicative of melting and recrystallisation processes which occur under the influence of the applied temperature and pressure during post-processing.

4.2. *Enhancing mechanism for interlaminar properties*

4.2.1. *Effect of PDA/NPs treatment on fibre/matrix interface*

The calculated adsorption energies for the interfaces of CF-SiO$_2$, CF-PDA, and PDA-SiO$_2$ provide a quantitative measure of the interaction strengths. MD simulations under an NVT ensemble at 298 K were carried out via Forcite module for 100 ps, allowed the systems to reach a fully relaxed state. The interfacial structures, as visualised in Fig. 5(a), reveal the relaxed configurations between carbon fibre and silica nanoparticles (CF-SiO$_2$), carbon fibre and polydopamine (CF-PDA), and polydopamine and silica nanoparticles (PDA-SiO$_2$), respectively. Upon obtaining stable adsorption configuration, the interaction energy ΔE was computed using Eq. (4):

$$\Delta E = E_{AB} - (E_A + E_B) \tag{4}$$

In this equation, E_{AB} represents the total energy of adsorption system comprising components A and B, while E_A and E_B denote the energies of the isolated component A and component B. The adsorption energies data during MD simulations, depicted in Fig. 5(a), indicate that CF-PDA interactions (-488 kcal/mol in average) were uniformly stronger than that involving SiO$_2$ (-287 kcal/mol in average). Notably, PDA displays a higher affinity for SiO$_2$ with an adsorption energy of -569 kcal/mol in average, suggesting that PDA significantly enhanced the surface interaction between CF and SiO$_2$. This stronger affinity between PDA and SiO$_2$ implies that PDA effectively enhanced the interface, leading to better adhesion and thus reinforcing the composite's structure. The energy profiles indicate that the presence of PDA created a more stable interface, contributing to the improved interlaminar properties observed

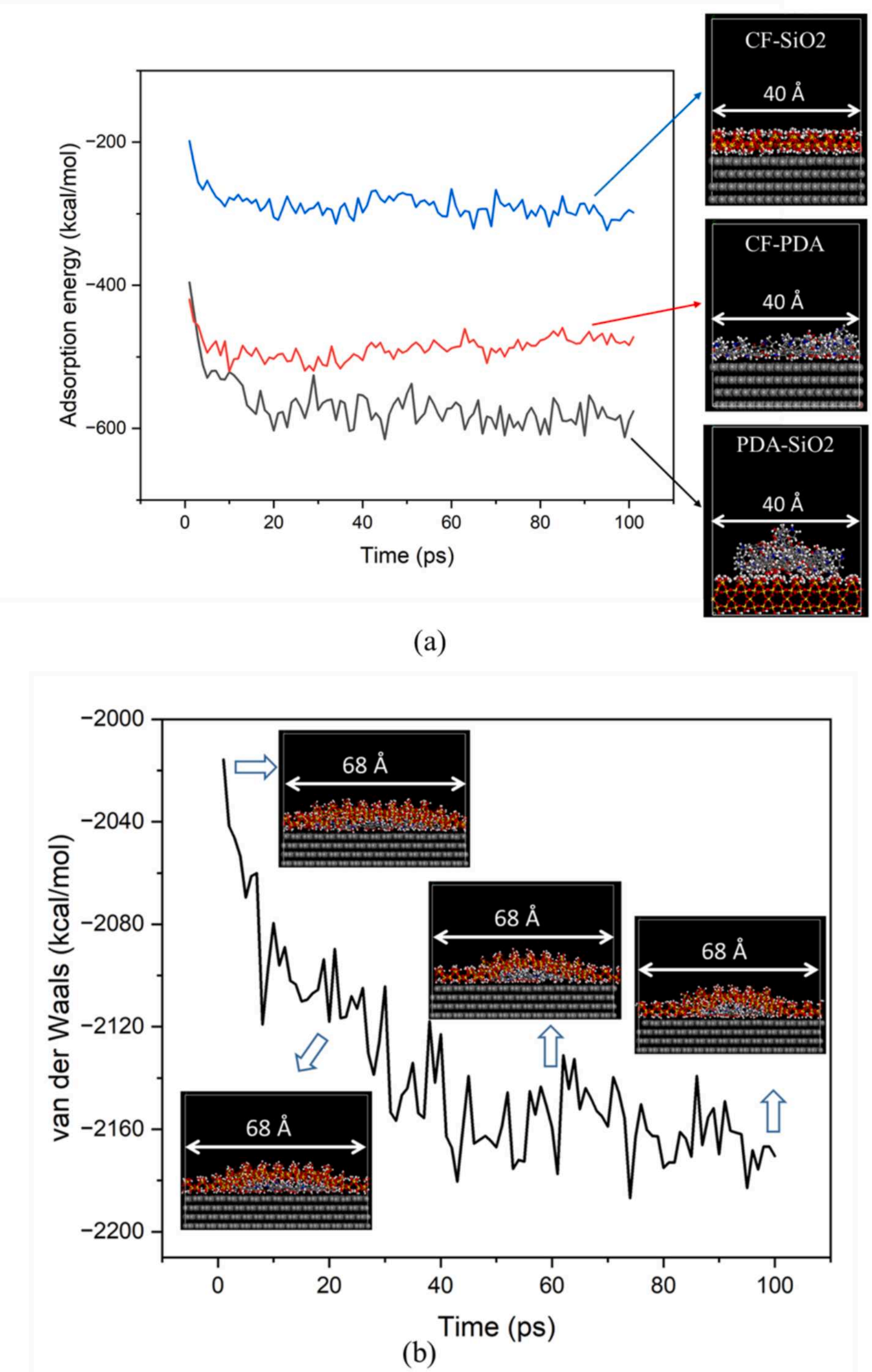

Fig. 5. (a) Adsorption energy and equilibrated models of CF-SiO_2, CF-PDA and PDA-SiO_2 in MD simulations; (b) changes in van der Waals force and morphology of models containing CF, PDA and SiO_2 layers over time during molecular dynamic adsorption progress in MD simulations.

in the enhanced composites.

A multi-layered system comprising PDA, SiO_2, and CF layers was constructed to investigate their stable adsorption configurations. The MD simulation was extended over 100 ps to monitor the adsorption progression and the change in van der Waals energies, which are depicted in Fig. 5(b). The sequential snapshots encapsulated within the figure shows the dynamic adsorption process, highlighting transitions in the interaction structure. As the simulation progresses, the silica nanoparticles exhibit an obvious affinity towards the PDA layer, progressively establishing a contact with the underlying carbon fibre surface. The role of PDA is crucial, serving as a binding agent that facilitates the adhesion of SiO_2 onto the CF substrate. This bridging effect not only stabilises the nanoparticle deposition but also enhances the surface properties of the carbon fibre, creating a modified interface with potentially superior mechanical attributes.

A detailed evaluation of the van der Waals in non-bonded energy components was also obtained via MD simulations. The simulation in Fig. 5(b) reveals a clear pattern: as the van der Waals forces get stronger, so does the bond between the particles. This shows that these forces are the primary driving force to make the combined material stable and strong. Essentially, the PDA acts as a connector, bringing together the silica and carbon fibre parts. The increase in van der Waals forces correlates with the strengthening of the adsorptive bond, suggesting a stronger connection over time. The whole process, captured by the simulation, emphasising the importance of van der Waals forces in explaining the role of PDA in binding the materials together, ultimately leading to a reinforced interface with enhanced material performance.

Fig. 6 illustrates the dynamic interfacial behaviour observed during fibre pull-out simulations, comparing two distinct models: one with untreated carbon fibre and the other with PDA/NPs treated carbon fibre. As the simulations advance, the untreated carbon fibre shows a clean separation from the PPS matrix, indicating minimal adhesion. In contrast, the treated carbon fibre retains a considerable amount of PPS matrix, attributed from the presence of hydroxyl (-OH) functional groups introduced by the PDA/NPs treatment.

The interfacial shear energy, defined as the peak energy required to disrupt the bond between the PPS matrix and the carbon fibre, is a measure of the energy difference throughout the pull-out process. Interfacial shear energy (W) is quantified by the energy variation and is given by the Eq. (5) [40]:

$$W = \frac{E_{max} - E_{min}}{A} \tag{5}$$

Here, W denotes the interfacial shear energy, E_{max} and E_{min} are the maximum and minimum potential energies of the total system, and L_x, A is the contact area, respectively.

The interfacial shear strength ($IFSS$) is expressed by the interfacial shear energy (W) as Eq. (6) [49]:

$$\tau_{IFSS} = kW = \delta[\frac{E_m}{E_f}]^{1/2}W \tag{6}$$

In this context, τ_{IFSS} represents the total interfacial shear strength, k is a coefficient of the proportionality between interfacial shear strength and interfacial shear energy. δ is the coefficient equal to about 2×10^9 m^{-1}, and E_m and E_f are the elastic moduli of PPS matrix and carbon fibre.

This equation reveals a linear relationship between the shear and the interfacial shear strength. Thus, the shear strength derived from nanoindentation experiments can be matched with the shear energy obtained from MD simulations.

The experimental results of single fibre push-out tests by nanoindentation ae depicted in Fig. 7(b) and (c). The microscopic images of single fibres after the push-out test are displayed in Fig. 7(e) and (f). As shown in Fig. 7(c), the representative force-displacement curves for composites reinforced with untreated carbon fibres and treated carbon fibres reached a plateau (marked with a dashed square) after an elastic deformation stage, which determines the maximum push-in force during the indenter displacement [34]. The first plateau in force-displacement curves was formed by the initial interface crack, which represents the elastic limits of the fibre/matrix bonding. It is obvious that the average interfacial shear strength (IFSS) of treated CF were higher than that of untreated CF (Fig. 7(b)). Results indicate that the stress was assumed to propagate directly through the smooth fibre/matrix interface in untreated composites, and the major failure was along the debonding fibre due to the poor fibre/matrix interface. After the treatment, however, the initial crack energy could be absorbed by silica nanoparticles deposited on the carbon fibre surface. The spherical shaped nanoparticles could

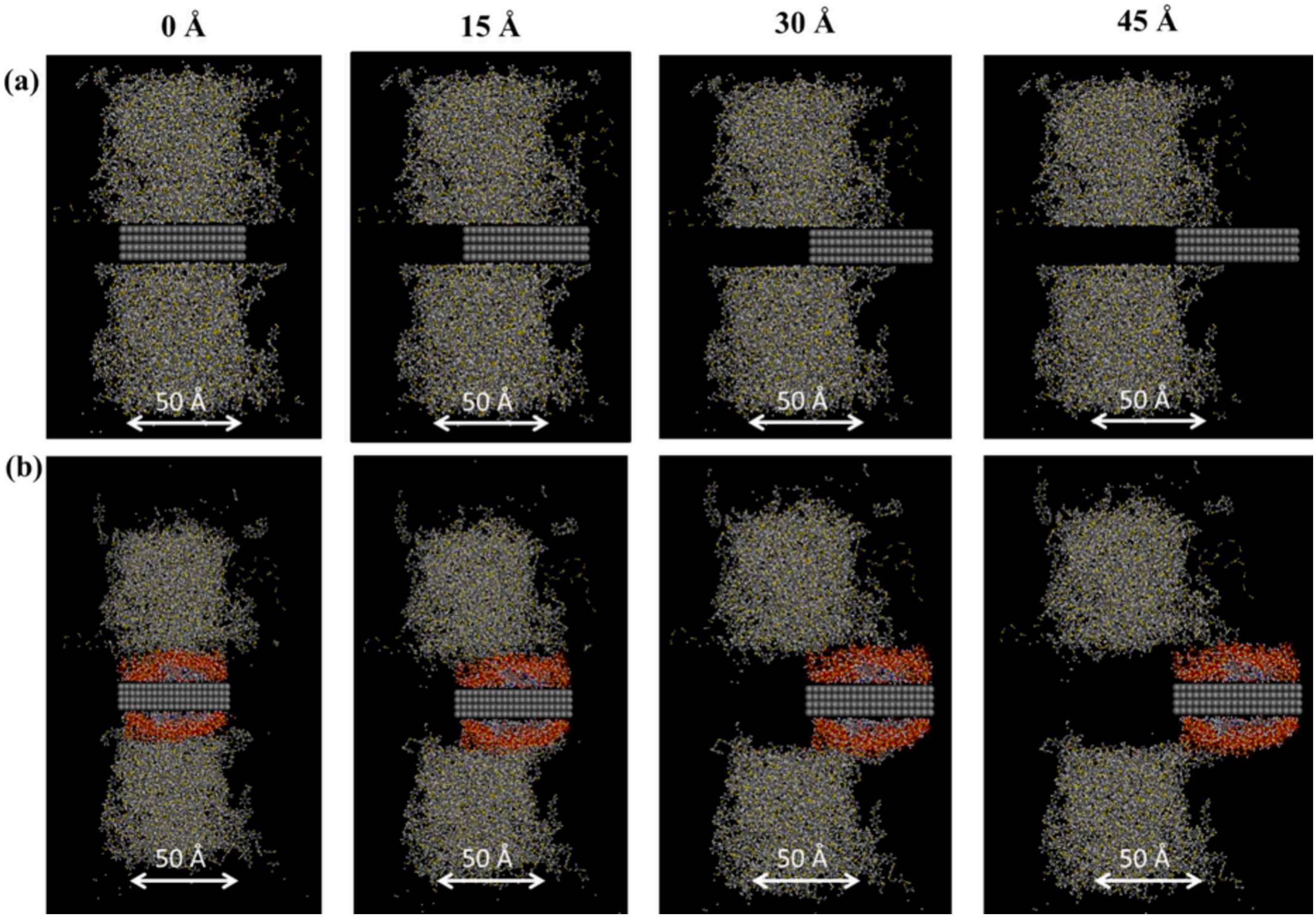

Fig. 6. The simulation of carbon fibre pull-out in CCF/PPS composites: (a) untreated carbon fibre; (b) treated carbon fibre.

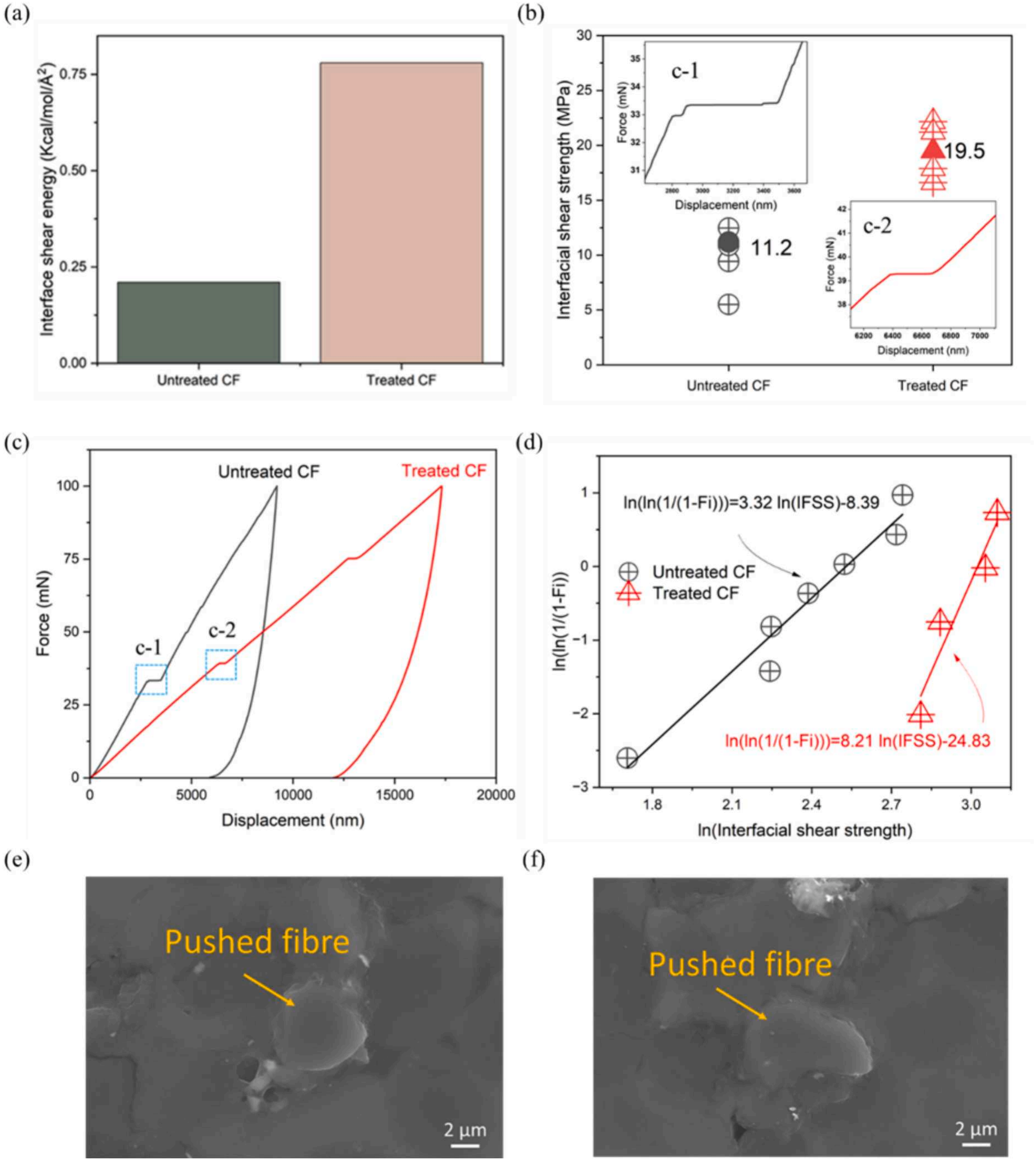

Fig. 7. (a) Simulated interface interaction energy calculated from the fibre pull-out shear simulations; (b) experimental interfacial shear strength (IFSS) from the single fibre push-out test; (c) representative force-depth curves in single fibre push-out test of composites reinforced with untreated CF (enlarged graph c-1) and treated CF (enlarged graph c-2); (d) Weibull plots of IFSS; (e) and (f) microscopic images of single fibres after the push-out test in treated composites.

induce small cracks in the interfacial region, acting as spacer, leading to a stress transfer in the interface region. As a result, the propagation of cracks would be retarded and fibre/matrix debonding would be prevented, contributing to an improved IFSS. In addition, a lower stiffness at the interface was found in the treated CF, compared with the untreated CF, which indicates that the interface has become more compliant or less rigid due to the treatment of PDA/NPs network. This could be the result of the treatment modifying the surface properties of carbon fibre, making the interface more capable of distributing stresses, which could better accommodate the deformations and contribute a tougher interface.

As shown in Fig. 7(a), the simulated untreated composite displays an interfacial shear energy of 0.21 kcal/mol/$Å^2$, whereas the treated composite exhibits a significantly higher value of 0.78 kcal/mol/$Å^2$. Correspondingly, the experimental IFSS values were also calculated from the plateau values of the force-depth curves. After the treatment of hybrid PDA/NPs network, the level of IFSS increased by 74.1%. A good consistence of nano-indentation results and MD simulations validates the reasonable simulations on interfacial adsorption and shear behaviour at nanoscale. Both results reveal the mechanism of PDA/NPs treatment on strengthening the fibre/matrix interface with interfacial bond and preventing interfacial failure with uniform deposition. The variability in IFSS values depicted in Fig. 7(b) is analytically represented by the Weibull equation [50].

$$P_F = 1 - exp\left[-\left(\frac{\tau_{IFSS}}{\tau_0}\right)^{\alpha}\right] \tag{7}$$

In this equation, P_F is the cumulative probability of interface failure in composite under a given IFSS, α is the Weibull modulus (a shape parameter) and τ_0 is the Weibull scale parameter. By taking the natural logarithm (twice) of both sides, the equation transforms to:

$$ln\left[ln\left(\frac{1}{1-F_i}\right)\right] = \alpha ln(\tau_{IFSS}) - \alpha ln(\sigma_0) \tag{8}$$

Here, F_i is the probability of failure at the i^{th} ranked specimen (ordered from lowest to highest strength), calculated as:

$$F_i = \frac{i-0.5}{N} \tag{9}$$

where N represents the total number of specimens. The Weibull plots of interfacial shear strength for composites with untreated CF and treated CF are shown in Fig. 7(d), where the calculated Weibull modulus α is 3.32 for untreated CF and 8.21 for treated CF. The presence of manufacturing-induced defects in carbon fibre filament, such as voids and non-impregnation between the carbon fibre and polymer matrix, contributes to the scattering in IFSS values. Consequently, the Weibull modulus α can be interpreted as a measure of the frequency distribution of these defects. Higher values of α suggest fewer defects and a more uniform distribution within the material [35,51]. This implies that composites reinforced with untreated CFs exhibited poorer impregnation, leading to greater variability in IFSS. On the contrary, the incidence of defects is reduced by grafting PDA/NPs hybrid network on the carbon fibre surface.

4.2.2. *Effect of post-processing on crystallinity and morphology*

Fig. 8 displays the DSC thermograms of specimens pre- and post-thermal processing. Employing Eq. (1), the percentage crystallinity of both sets of specimens was calculated. The DSC curves reveal notable distinctions in the melting peak profiles: post-processed specimens exhibit broader peaks with a larger integrated area, indicative of heightened crystallinity. This observation is quantified by an increase in the crystallinity, which rises from 35.6% in the as-printed specimens to a higher percentage of 59.8% following post-processing, showing that more organised crystalline structures are formed. The observed enlargement in peak breadth and area under the curve is indicative of an enhanced degree of order within the polymer matrix, resulting from the post-processing conditions at elevated temperature and pressure. The more organised polymer chains within the matrix indicate a transformation in microstructural integrity. Specifically, this rearrangement of polymer chains in the matrix translates to stronger interlaminar shear strength (ILSS), resulting from improved load transfer from the polymer to the fibres. The results suggest that the application of specific thermal and pressure conditions can enhance the mechanical robustness of the material.

Additionally, the cross-sectional images observed by optical microscope and SEM are shown in Fig. 9. The images illustrate a significant reduction in voids after applying a moderate pressure (1 MPa) to the specimens. This consolidation effect has led to a considerable decrease in void content, from 10.2% in the as-printed specimen to 3.4% in the post-processed specimen, as quantified by ImageJ software analysis. Consequently, the volume fraction of carbon fibre slightly increases from 50.9% to 54.6% after hot-press compression. As a result, the reduction in voids minimises the defects at the layer-layer interfaces, thereby strengthening the interlaminar shear strength. Furthermore, the consolidation process has been shown to further potentially improve the orientation of continuous carbon fibre compared to the as-printed specimens. Overall, post-processing has demonstrably enhanced both the interlaminar properties and the material's resistance to deformation under shear and flexural stresses.

4.2.3. *Synergistic effect on interlaminar properties*

To further elucidate the impact of carbon fibre treatment and post-processing on the interlaminar properties, X-ray computed tomography (XCT) images of failure modes following the short-beam shear tests on 3D printed CCF/PPS specimens were presented in Fig. 10. Generally, the printed parts undergoing testing exhibited an inelastic deformation and ductility. A prevalent mode of failure identified in the composites was delamination, as evidenced in both composites reinforced with pristine carbon fibre (p-CCF/PPS) and treated carbon fibre (t-CCF/PPS), depicted in Fig. 10(a) and (b). In contrast, the post-processed composites post processed at elevated temperatures and pressures demonstrated more intricate failure modes. Beyond interlayer delamination, the specimens also exhibited tension and compression failures, as illustrated in Fig. 10(c) and (d).

Furthermore, the mechanical response of carbon fibre treatment positively correlated with the failure modes at the interlaminar level. When comparing untreated specimens to treated ones, it was observed that cracks propagated more uniformly through the fibre/matrix interface in the untreated composites. The combined effects of the PDA/NPs network on the carbon fibre surface and the post-processing techniques are promising in enhancing the shear yield stress at the interface layer. Consequently, these improvements lead to significantly enhanced interlaminar properties of the composites.

The fracture surfaces of the CF/PPS composites following the ILSS test were examined in Fig. 11 to further explore the synergistic effect of

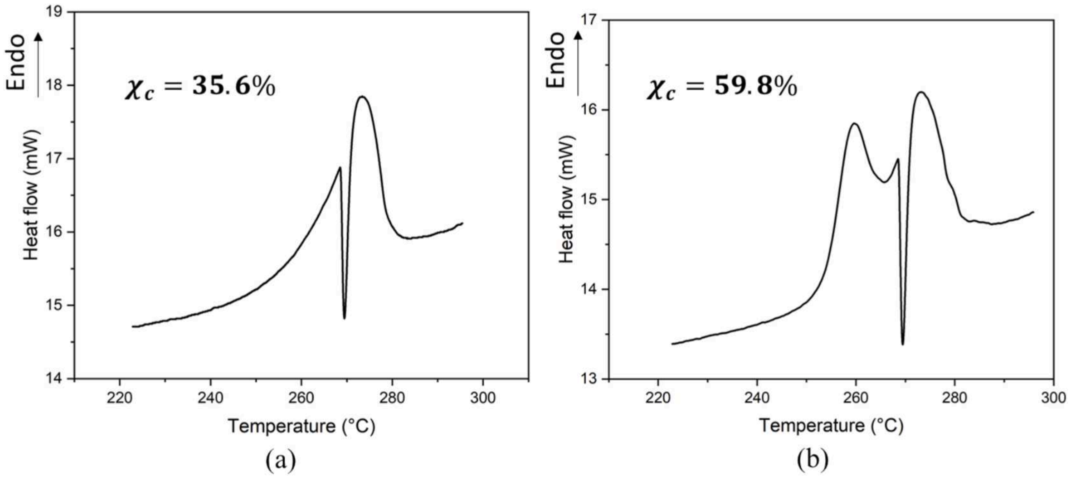

Fig. 8. DSC curves of CCF/PPS composites: (a) as-printed and (b) post-processed.

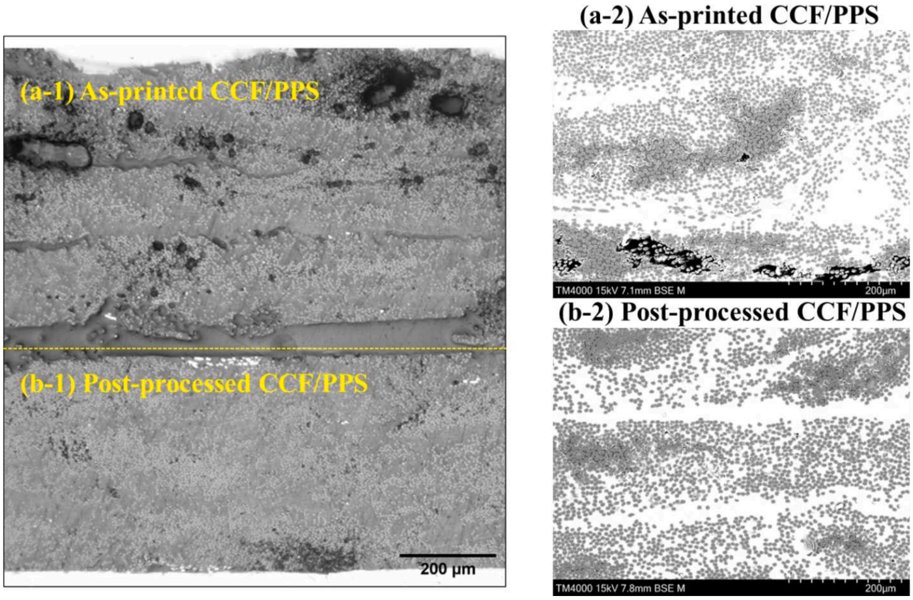

Fig. 9. Microscopic images of as-printed (a-1: optical image; a-2: SEM image) and post-processed (b-1: optical image; b-2: SEM image) CCF/PPS composites.

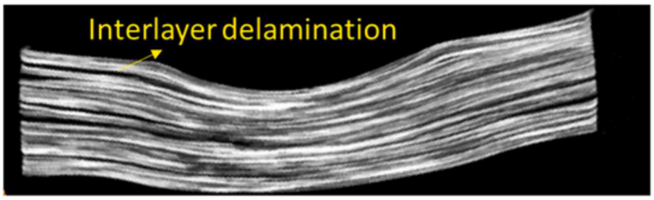

(a) p-CCF/PPS

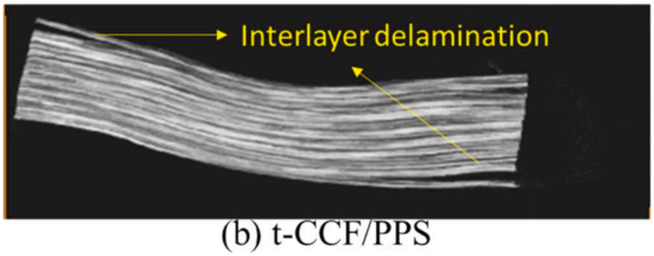

(b) t-CCF/PPS

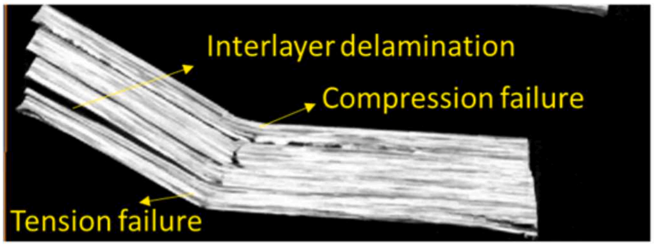

(c) ph-CCF/PPS

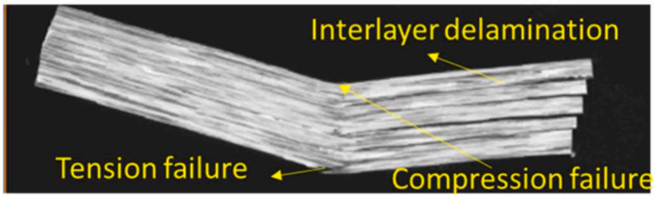

(d) th-CCF/PPS

Fig. 10. XCT imaging of (a) p-CCF/PPS, (b) t-CCF/PPS, (c) th-CCF/PPS and (d) ph-CCF/PPS.

improving the fibre/matrix interfacial and interlayer properties through the incorporation of PDA/NPs network and subsequent post-processing techniques. Upon examining p-CCF/PPS (Fig. 11(a)) and its zoomed-in image, it was observed that the untreated carbon fibres were predominantly detached from the PPS matrix across many surface areas, attributing to weaker interfacial adhesion. This was evidenced by the observation of clean and smooth fibre bundles and gaps aligned with the CF direction, suggesting rapid crack propagation through the CF/PPS interface. Following the integration of the PDA/NPs network to t-CCF/PPS (refer to Fig. 11(b)), an obvious layer of PPS resin was found on the fractured surface, alongside more textured CF surface patterns. In this context, the silica nanoparticles functioned as spacers in the interfacial region, promoting the development of multiple smaller cracks rather than direct debonding between the PPS matrix and carbon fibres.

Compared to p-CCF/PPS (Fig. 11(a)), an increased impregnation percentage was observed in ph-CCF/PPS (Fig. 11(b)), expanding the area of matrix residue present during the separation process. This improvement results from the void compaction and partial crystallinity rearrangement during the post-printing compression. Compared to ph-CCF/PPS (see Fig. 11(c)), a more obvious zigzag fracture pattern between carbon fibres and the PPS matrix for th-CCF/PPS was depicted in Fig. 11(d), which was attributed by a synergistic effect of surface treatment during the filament fabrication. The compatible coating provides functional groups on the CF and further promotes better bonding at the fibre/matrix interface as compression ensures thorough contact and bonding. Additionally, these treatments lead to favourable wetting of fibres within the matrix, further optimised by the compaction of interlayers. With improved fibre-matrix adhesion and reduced internal defects, the composite can withstand higher loads and exhibits enhanced performance under stress. These synergistic effects result in well-bonded and densely structured composites with improved load transfer capabilities, contributing to enhanced shear yield stress within the interface layer.

4.3. Post-processing of complex CCF/PPS composite structures using a salt-bath

It is known that 3D printing has advantages for manufacturing complex structures. Therefore, it is expected that a low-cost post-processing method would benefit its application to more complex structures. Here, we propose a novel post-processing method with salt bath

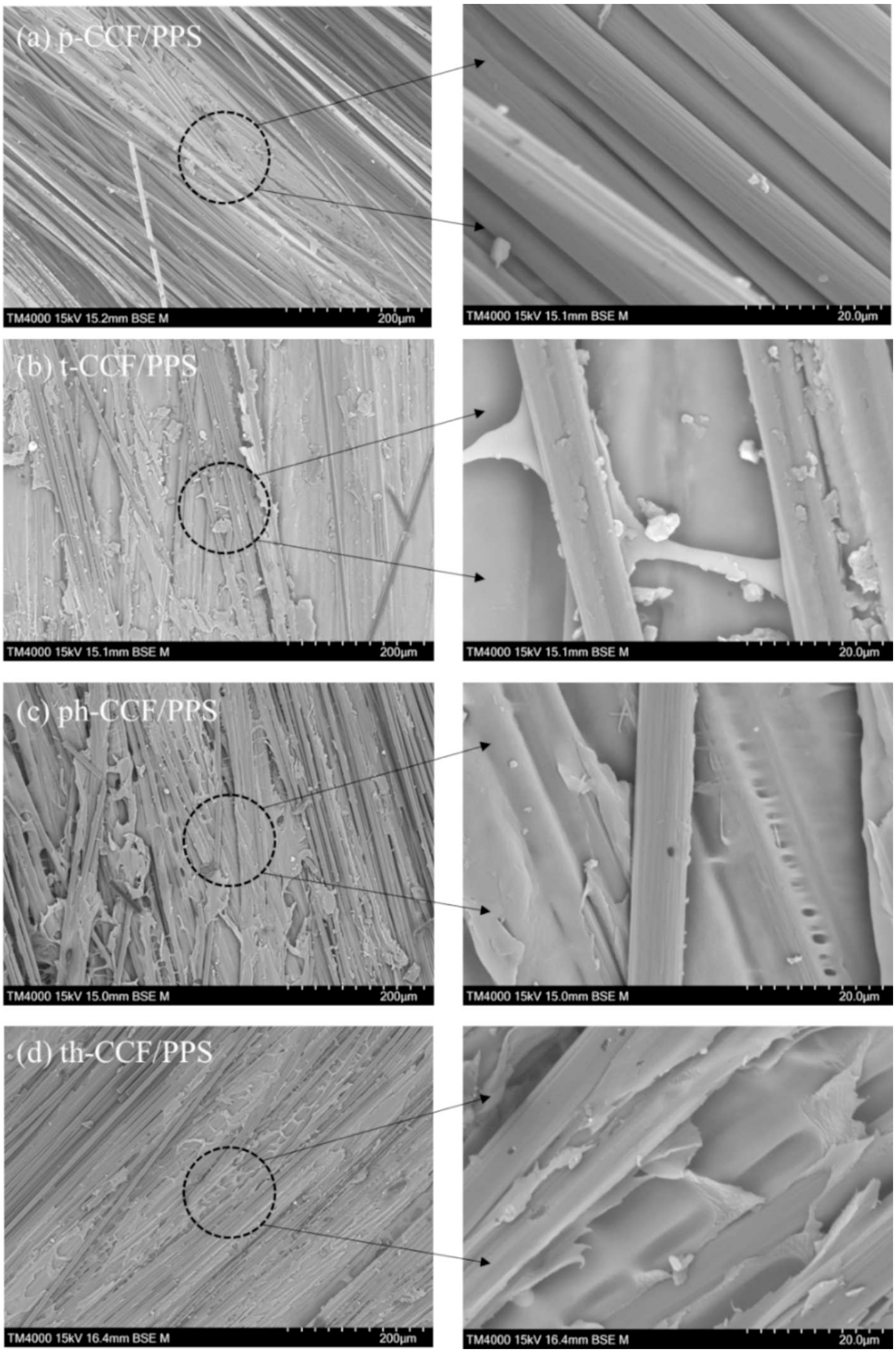

Fig. 11. SEM images of (a) p-CCF/PPS, (b) t-CCF/PPS, (c) th-CCF/PPS and (d) ph-CCF/PPS (left: ×500; right: ×5000).

for 3D printed CCF/PPS composite structures with complex geometries. The pressure in the salt bath process is applied hydrostatically by the top plate of the cuboid metal mould. The composites samples are submerged in the bath of hot salt, which is maintained at a specified temperature. The nature of the hot salt allows for even distribution of pressure around the composite material as the salt conforms to the shape of the sample. After the completion of compression, the samples were carefully removed from the hot salt and allowed to cool slightly. Then, the salt adhering to the surface of the composites is mechanically brushed off. The final traces of salt are dissolved and removed by rinsing the samples with water and then dry completely in the oven to ensure that no residual salt remains.

Fig. 12 presents the force-displacement curves in short-beam bending for carbon fibre-reinforced polyphenylene sulphide (PPS) composites subjected to different post-processing techniques. The graph compares the peak force of as-printed specimens against those that have undergone post-processing using a specifically designed metal mould and a salt bath method. The composites post-processed with the salt bath generally falls below that of the mould-processed counterparts but remains superior to the as-printed composites. This trend holds true for both untreated and treated CCF/PPS composites. Notably, both post-processed curves start with a similar initial modulus, indicating comparable stiffness at the onset of loading. The curves reveal that while the mould-based post-processing technique leads to higher peak values, the salt bath method exhibits a more pronounced plastic deformation beyond the peak, similar to the behaviour of the as-printed specimen.

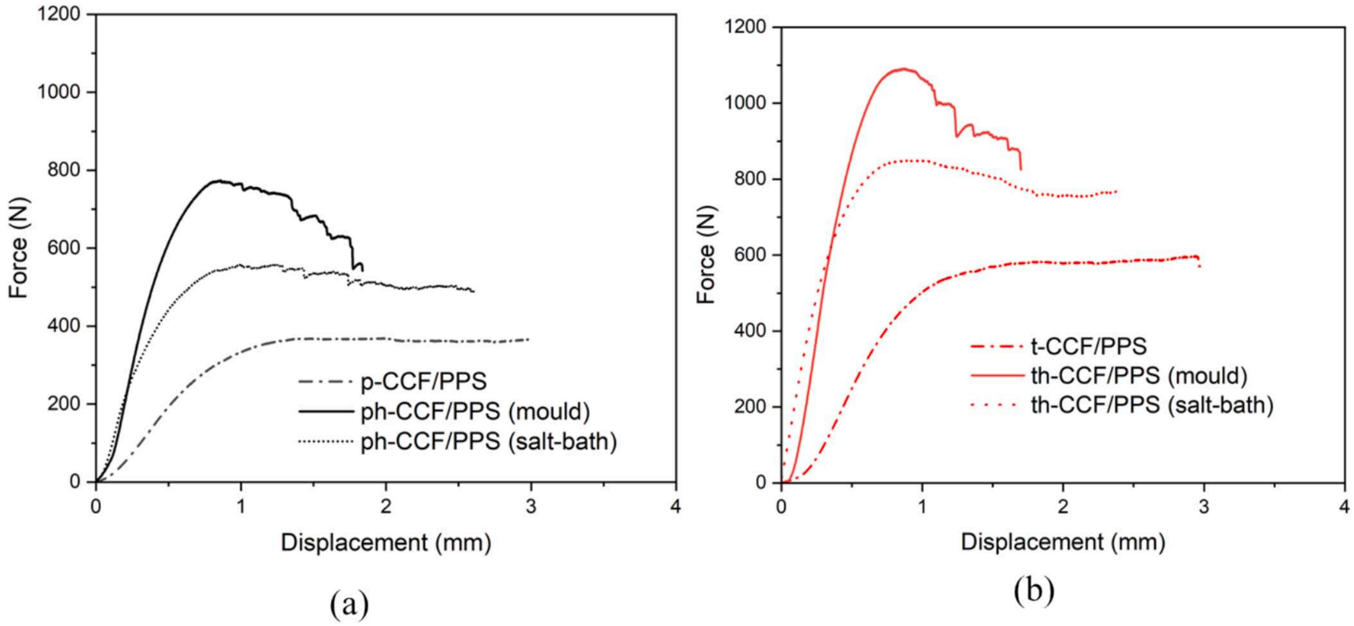

Fig. 12. Representative force-displacement curves in short beam bending for specimens before and after mould-based hot press and salt-bath based hot press (a-untreated composites; b-treated composites).

This suggests that the salt bath post-processing not only retains some of the ductility seen in the as-printed composites but also enhances the interlaminar properties.

The use of a salt bath for post-processing is particularly advantageous for complex geometries. During hot pressing, the salt acts as a support, enabling the precise shaping of intricate two-dimensional perforated patterns and three-dimensional structures. This technique ensures that even with the application of high temperatures and moderate pressures, the integrity of the complex designs is maintained. In summary, the salt bath post-processing method emerges as an effective alternative to traditional mould methods, offering a balanced improvement in interlaminar properties. It aligns with the strengths of 3D printing in manufacturing complex structures, allowing for the retention of design intricacies while enhancing material performance.

We further demonstrated the effect of the salt-bath based post-processing on two demonstrative models with complex geometries, a two-dimensional lightweight perforated structure featuring an array of holes (Fig. 13) and a three-dimensional integrated stiffener structure (Fig. 14), respectively. Pre-treated CCF/PPS filament was used in printing these demonstrative models. The former design, depicted in Fig. 13, is typically challenging to post-process due to the risk of distorting the delicate features. Fig. 13(a) shows the printing trajectory of the model. The dimensions of components, pre- and post-hot pressing, were quantified using a FARO arm scanner to capture precise geometry and assess dimensional variances. Observations from Fig.13 (c) and (d) reveal that the fitting ellipse for the as-printed part measured a major axis of 119.11 mm and a minor axis of 12.88 mm, whereas post-processing dimensions registered a major axis of 119.18 mm and minor axis of 13.22 mm. These corresponding deviations are less than 2%, shown in Table S2. A notable reduction in thickness by 10.4% in post-pressing samples shows a decrease in void content within the composites, and the change in the width (labelled in Fig. 13(b)) have a reduction by 9.4%. The salt-bath based post-processing has been validated to preserve the integrity of these perforations while reducing the defects in all directions due to flexibility of salt.

The other case, shown in Fig. 14, is a three-dimensional stiffener structure. The complexity of this geometry, with its integrated layers and support elements, often complicates post-processing. For the as-printed part, presented in Fig. 14 (c), the top inner diameter measured 170.29 mm, and the top outer diameter stood at 190.83 mm. Correspondingly, the bottom inner diameter was 200.29 mm, and the bottom diameter measured 165.37 mm. Post-processed dimensions, as shown in Fig. 14 (d), indicated a top inner diameter of 169.80 mm and a top outer diameter of 188.84 mm. Correspondingly, the diameters of bottom inner and bottom outer measured 199.37 mm and 165.38 mm, respectively. All calculated deviations of as-printed part and post-processed part based on nominal dimensions in the top and bottom sections are less than 2%, shown in Table S3. An expected reduction in thickness by 13.1% is in the post-processed part, which also validate the void minimisation of the composites. Notably, the top width has decreased by 7.3% due to the reduction of voids as well, which results from the pressure distributed in the in-plane direction. The findings demonstrate that the salt-bath approach effectively mitigates the structural defects in both out-of-plane and in-plane directions.

These two demonstrations illustrate that the salt-bath based post-processing technique is advantageous for complex structures that benefit from the design freedom of 3D printing. This method offers a post-processing solution that upholds the dimensional accuracy and design intricacy of printed objects while delivering an improvement in mechanical performance. The post-processing technique applied to 3D printed composites shows promise in enhancing the interlaminar properties for both uncomplicated shapes using a mould-based method and complex structures via the salt-bath technique. Furthermore, surface quality of the as-printed parts and post-processed parts was characterised by the SEM micrographs (refer to Fig. S4). The results show that, despite the applied pressure and temperature enabling the matrix material to fill in the voids and enhance impregnation into fibre bundles, unfilled gaps and uneven continuous fibres in the post-processed parts using a salt bath still contribute to high surface roughness. Therefore, surface quality needs to be further improved in this procedure to meet higher surface quality requirements.

5. Conclusions

The study elucidates the considerable advantages of PDA/NPs treatment and post-processing techniques on the mechanical performance of CCF/PPS composites. Specifically, the introduction of silica nanoparticles and polydopamine hybrid network treatment on

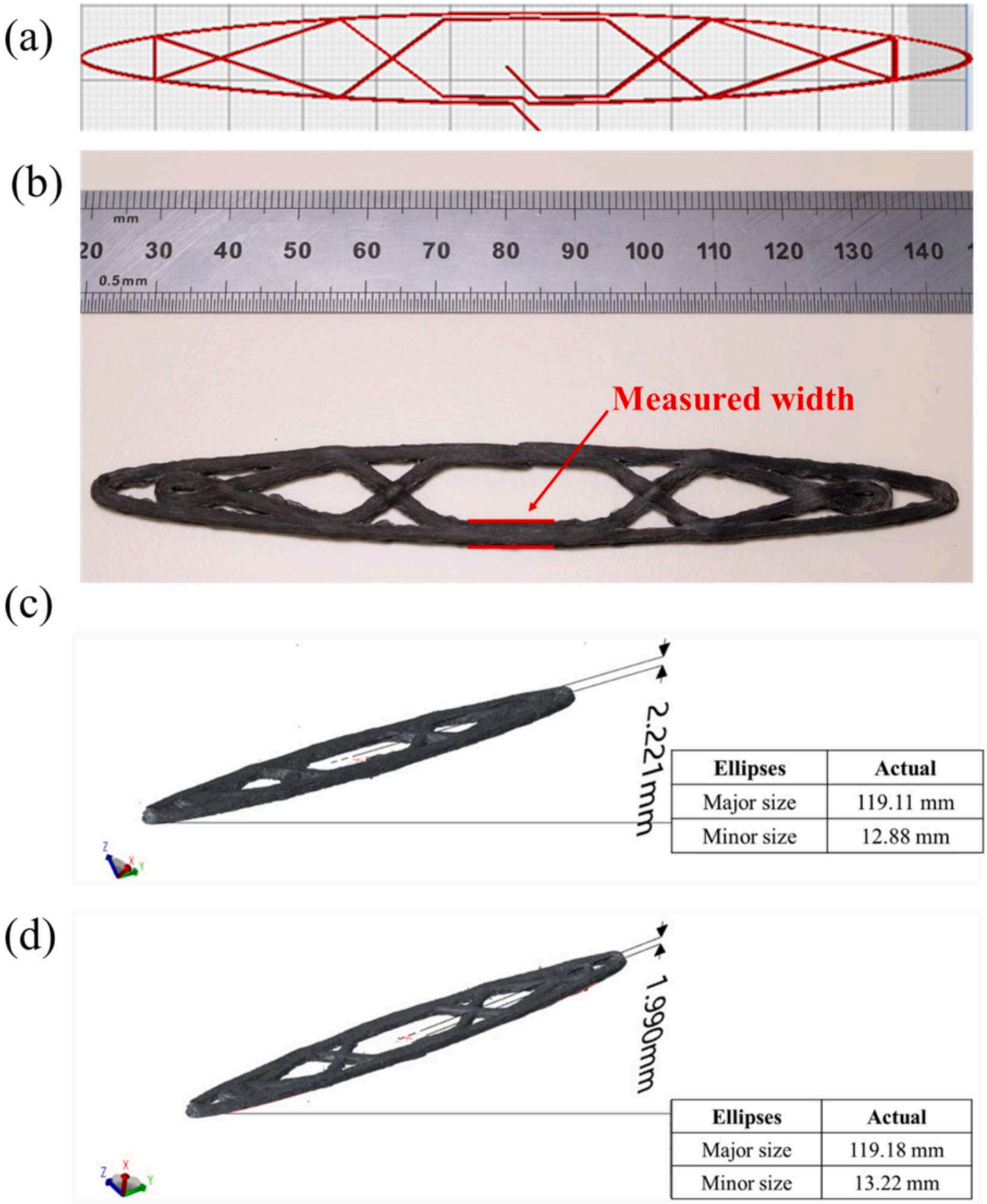

Ellipses	Actual
Major size	119.11 mm
Minor size	12.88 mm

Ellipses	Actual
Major size	119.18 mm
Minor size	13.22 mm

Fig. 13. Demonstration of a perforated structure using the salt-bath method: (a) designed trajectory of continuous carbon fibre; (b) image of post-processed part; (c) scanning of as-printed part; (d) scanning of post-pressed part.

commercial carbon fibres improves fibre/matrix adhesion, a fundamental issue that has limited the performance of 3D printed CCRTP. The development and validation of optimised post-processing method using a salt bath for 3D printed complex structures effectively mitigate the defects related to layer adhesion. In addition, this paper performs a comprehensive analysis at the molecular and microstructural level, providing a deep understanding of the mechanisms of the synergistic effects of these treatments.

The integration of PDA/NPs network on CCF and post-processing technique have been proven to significantly enhance the interfacial and interlayer properties. This has led to a substantial improvement of 27% in flexural strength and 172% in the interlaminar shear strength (ILSS). For the effect of PDA/NPs treatment, the MD simulations offered further insights into the enhanced adhesion mechanisms, validating the experimental observations in the nano-indentation test. For the effect of post-processing techniques, the DSC analysis and morphological observations confirmed improvements in crystallinity, void content reduction and fibre orientation, which correlated with the superior mechanical performance under shear and flexural loads. Moreover, a salt-bath based post-processing technique was shown to successfully preserve the intricate details of complex 3D printed structures while enhancing their material mechanical performance. These findings not only provide a deeper understanding of the interfacial and interlayer properties of 3D printed CCF/PPS composites but also demonstrates practical enhancements that can be readily applied in aerospace and automotive industries, where high-performance thermoplastic composite materials are advantageous.

CRediT authorship contribution statement

Yahui Lyu: Writing – original draft, Methodology, Formal analysis, Data curation. **Aonan Li:** Resources, Methodology. **Jiang Wu:**

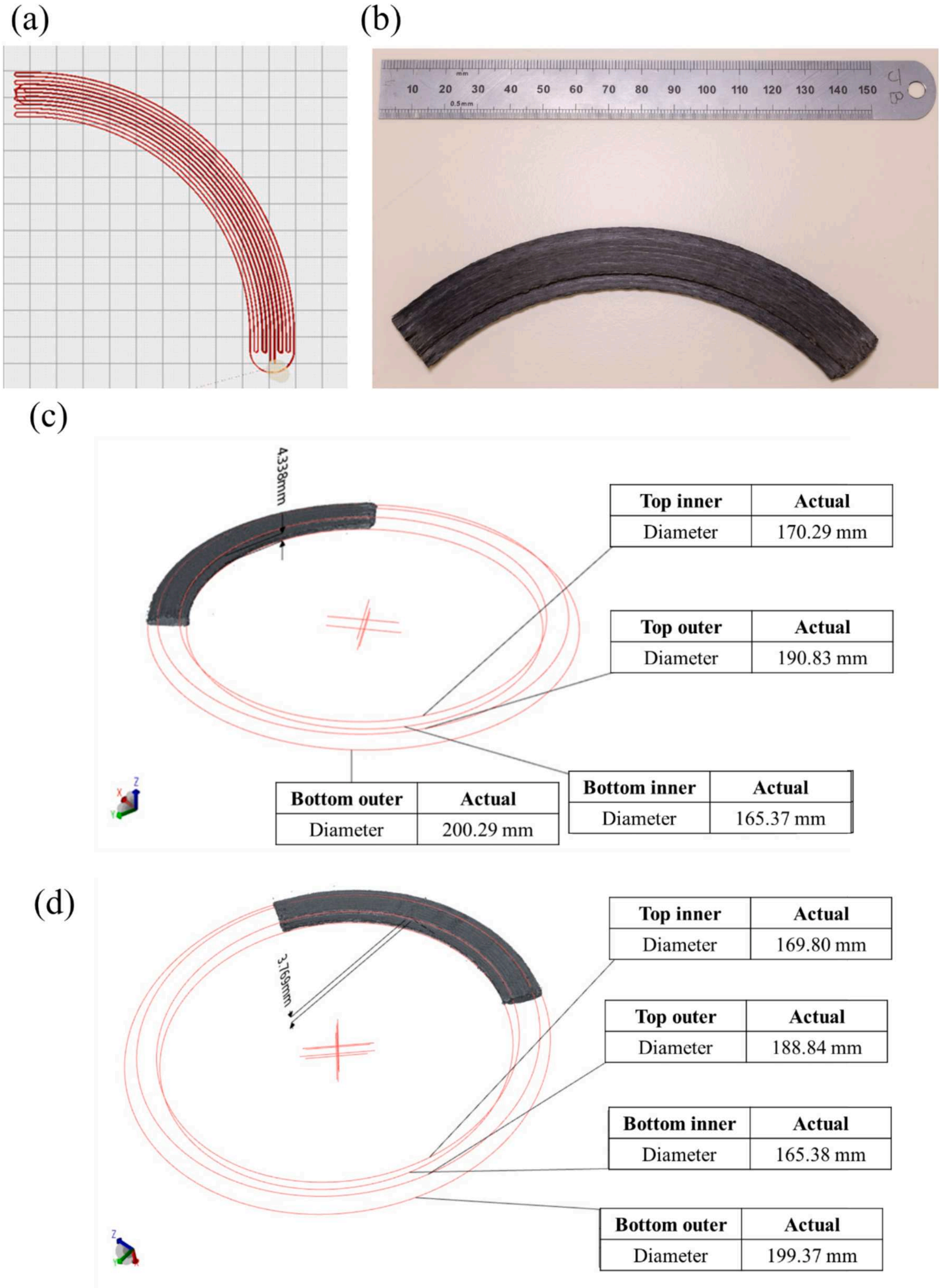

Fig. 14. Demonstration of an integrated stiffener structure using the salt-bath method: (a) designed trajectory of continuous carbon fibre; (b) image of post-processed part; (c) scanning of as-printed part; (d) scanning of post-processed part.

Visualization, Resources. **Vasileios Koutsos:** Writing – review & editing, Supervision. **Chun Wang:** Supervision, Data curation. **Conchúr M.Ó. Brádaigh:** Writing – review & editing, Supervision. **Dongmin Yang:** Writing – review & editing, Supervision, Conceptualization.

Declaration of competing interest

The authors declare that they have no known competing financial interests or personal relationships that could have appeared to influence the work reported in this paper.

Acknowledgements

The authors would like to acknowledge Andrew Brown at the School of Engineering, University of Edinburgh for assistance with FARO arm scanner, and the Institute for Condensed Matter Physics and Complex Systems at the University of Edinburgh for Avizo software used in this research. The authors would like to extend their gratitude to Prof. Xiangcheng Li at Wuhan University of Science and Technology for Materials Studio software used in the simulation. Yahui Lyu would like to acknowledgment Edinburgh Global Research Scholarship and the Principal's Career Development Scholarship for financial support of her PhD study. For the purpose of open access, the authors have applied a Creative Commons Attribution (CC BY) license to any author accepted manuscript version arising from this submission.

Appendix A. Supplementary data

Supplementary data to this article can be found online at https://doi.org/10.1016/j.compositesa.2024.108627.

Data availability

Data will be made available on request.

References

[1] Yao SS, Jin FL, Rhee KY, Hui D, Park SJ. Recent advances in carbon-fiber-reinforced thermoplastic composites: A review. Compos B Eng 2018;142:241–50. https://doi.org/10.1016/j.compositesb.2017.12.007.

[2] Araya-Calvo M, López-Gómez I, Chamberlain-Simon N, León-Salazar JL, Guillén-Girón T, Corrales-Cordero JS, et al. Evaluation of compressive and flexural properties of continuous fiber fabrication additive manufacturing technology. Addit Manuf 2018;22:157–64. https://doi.org/10.1016/j.addma.2018.05.007.

[3] Parker M, Ezeokeke N, Matsuzaki R, Arola D. Strength and its variability in 3D printing of polymer composites with continuous fibers. Mater Des 2023;225. https://doi.org/10.1016/j.matdes.2022.111505.

[4] Wu S, Shan Z, Chen K, Liu X, Jiang X, Wang S, et al. Investigation of bending properties of continuous fiber reinforced resin T-beams made by 3D printing. Structures 2023;50:835–41. https://doi.org/10.1016/j.istruc.2023.01.034.

[5] Valente M, Rossitti I, Sambucci M. Different Production Processes for Thermoplastic Composite Materials: Sustainability versus Mechanical Properties and Processes Parameter. Polymers (Basel) 2023;15. https://doi.org/10.3390/polym15010242.

[6] Vaidya UK, Chawla KK. Processing of fibre reinforced thermoplastic composites. International Materials Reviews 2008;53:185–218. https://doi.org/10.1179/174328008X325223.

[7] Steggall-Murphy C, Simacek P, Advani SG, Yarlagadda S, Walsh S. A model for thermoplastic melt impregnation of fiber bundles during consolidation of powder-impregnated continuous fiber composites. Compos Part A Appl Sci Manuf 2010;41:93–100. https://doi.org/10.1016/j.compositesa.2009.09.026.

[8] Ouagne P, Bizet L, Baley C, Bréard J. Analysis of the film-stacking processing parameters for PLLA/flax fiber biocomposites. J Compos Mater 2010;44:1201–15. https://doi.org/10.1177/0021998309349019.

[9] Aisyah HA, Paridah MT, Sapuan SM, Ilyas RA, Khalina A, Nurazzi NM, et al. A comprehensive review on advanced sustainable woven natural fibre polymer composites. Polymers (Basel) 2021;13:1–45. https://doi.org/10.3390/polym13030471.

[10] Goud V, Alagirusamy R, Das A, Kalyanasundaram D. Influence of various forms of polypropylene matrix (fiber, powder and film states) on the flexural strength of carbon-polypropylene composites. Compos B Eng 2019;166:56–64. https://doi.org/10.1016/j.compositesb.2018.11.135.

[11] Van de Werken N, Tekinalp H, Khanbolouki P, Ozcan S, Williams A, Tehrani M. Additively manufactured carbon fiber-reinforced composites: State of the art and perspective. Addit Manuf 2020;31:100962. https://doi.org/10.1016/j.addma.2019.100962.

[12] Blok LG, Longana ML, Yu H, Woods BKS. An investigation into 3D printing of fibre reinforced thermoplastic composites. Addit Manuf 2018;22:176–86. https://doi.org/10.1016/j.addma.2018.04.039.

[13] Xu W, Jambhulkar S, Zhu Y, Ravichandran D, Kakarla M, Vernon B, et al. 3D printing for polymer/particle-based processing: A review. Compos B Eng 2021;223. https://doi.org/10.1016/j.compositesb.2021.109102.

[14] Ngo TD, Kashani A, Imbalzano G, Nguyen KTQ, Hui D. Additive manufacturing (3D printing): A review of materials, methods, applications and challenges. Compos B Eng 2018;143:172–96. https://doi.org/10.1016/j.compositesb.2018.02.012.

[15] Kumar V, Alwekar SP, Kunc V, Cakmak E, Kishore V, Smith T, et al. High-performance molded composites using additively manufactured preforms with controlled fiber and pore morphology. Addit Manuf 2021;37:101733. https://doi.org/10.1016/j.addma.2020.101733.

[16] Tekinalp HL, Kunc V, Velez-Garcia GM, Duty CE, Love LJ, Naskar AK, et al. Highly oriented carbon fiber-polymer composites via additive manufacturing. Compos Sci Technol 2014;105:144–50. https://doi.org/10.1016/j.compscitech.2014.10.009.

[17] Hassen AA, Lindahl J, Chen X, Post B, Love L, Kunc V. Additive manufacturing of composite tooling using high temperature thermoplastic materials. In: SAMPE Conference Proceedings, Long Beach, CA; 2016. p. 2648–58.

[18] Heidari-Rarani M, Rafiee-Afarani M, Zahedi AM. Mechanical characterization of FDM 3D printing of continuous carbon fiber reinforced PLA composites. Compos B Eng 2019;175. https://doi.org/10.1016/j.compositesb.2019.107147.

[19] Tambrallimath V, Keshavamurthy R, Saravanabavan D, Koppad PG, Kumar GP. Thermal behavior of PC-ABS based graphene filled polymer nanocomposite synthesized by FDM process. Composites Communications 2019;15:129–34. https://doi.org/10.1016/j.coco.2019.07.009.

[20] Yin J, Lu C, Fu J, Huang Y, Zheng Y. Interfacial bonding during multi-material fused deposition modeling (FDM) process due to inter-molecular diffusion. Mater Des 2018;150:104–12. https://doi.org/10.1016/j.matdes.2018.04.029.

[21] de Toro EV, Sobrino JC, Martínez AM, Eguía VM, Pérez JA. Investigation of a short carbon fibre-reinforced polyamide and comparison of two manufacturing processes: Fused Deposition Modelling (FDM) and polymer injection moulding (PIM). Materials 2020;13. https://doi.org/10.3390/ma13030672.

[22] Safari F, Kami A, Abedini V. 3D printing of continuous fiber reinforced composites: A review of the processing, pre- and post-processing effects on mechanical properties. Polymers and Polymer Composites 2022;30. https://doi.org/10.1177/09673911221098734.

[23] Li S, Wang K, Zhu W, Peng Y, Ahzi S, Chinesta F. Contributions of interfaces on the mechanical behavior of 3D printed continuous fiber reinforced composites. Constr Build Mater 2022;340. https://doi.org/10.1016/j.conbuildmat.2022.127842.

[24] Wu Q, Wan Q, Yang X, Wang F, Bai H, Zhu J. Remarkably improved interfacial adhesion of pitch-based carbon fiber composites by constructing a synergistic hybrid network at interphase. Compos Sci Technol 2021;205:108648. https://doi.org/10.1016/j.compscitech.2021.108648.

[25] Eyckens DJ, Arnold CL, Simon Ž, Gengenbach TR, Pinson J, Wickramasingha YA, et al. Covalent sizing surface modification as a route to improved interfacial adhesion in carbon fibre-epoxy composites. Compos Part A Appl Sci Manuf 2021;140. https://doi.org/10.1016/j.compositesa.2020.106147.

[26] He Q, Wang H, Fu K, Ye L. 3D printed continuous CF/PA6 composites: Effect of microscopic voids on mechanical performance. Compos Sci Technol 2020;191. https://doi.org/10.1016/j.compscitech.2020.108077.

[27] Barocio E, Brenken B, Favaloro A, Bogdanor M, Pipes RB. Extrusion deposition additive manufacturing with fiber-reinforced thermoplastic polymers. In: Structure and properties of additive manufactured polymer components. Woodhead Publishing; 2020. p. 191–219. https://doi.org/10.1016/B978-0-12-819535-2.00007-7.

[28] Gao X, Qi S, Kuang X, Su Y, Li J, Wang D. Fused filament fabrication of polymer materials: A review of interlayer bond. Addit Manuf 2021;37. https://doi.org/10.1016/j.addma.2020.101658.

[29] Pascual-González C, San Martín P, Lizarralde I, Fernández A, León A, Lopes CS, et al. Post-processing effects on microstructure, interlaminar and thermal properties of 3D printed continuous carbon fibre composites. Compos B Eng 2021;210. https://doi.org/10.1016/j.compositesb.2021.108652.

[30] Bhandari S, Lopez-Anido RA, Gardner DJ. Enhancing the interlayer tensile strength of 3D printed short carbon fiber reinforced PETG and PLA composites via annealing. Addit Manuf 2019;30. https://doi.org/10.1016/j.addma.2019.100922.

[31] Lyu Y, Koutsos V, Brádaigh CMÓ, Yang D. Improving the interfacial adhesion between recycled carbon fibres and polyphenylene sulphide by bio-inspired dopamine for advanced composites manufacturing. J Clean Prod 2024;449:141855. https://doi.org/10.1016/j.jclepro.2024.141855.

[32] Ibrahim IA, Zikry AAF, Sharaf MA. Preparation of spherical silica nanoparticles: Stober silica. J. Am. Sci 2010;6(11):985–9.

[33] Zhang H, Zhang K, Li A, Wan L, Robert C, Brádaigh CMÓ, et al. 3D printing of continuous carbon fibre reinforced powder-based epoxy composites. Composites Communications 2022;33. https://doi.org/10.1016/j.coco.2022.101239.

[34] Zhang L, Ren C, Zhou C, Xu H, Jin X. Single fiber push-out characterization of interfacial mechanical properties in unidirectional CVI-C/SiC composites by the nano-indentation technique. Appl Surf Sci 2015;357:1427–33. https://doi.org/10.1016/j.apsusc.2015.10.018.

[35] M.A. Yan, Mechanical characterization and fracture behavior of thermosetting and thermoplastic polymer based carbon fiber reinforced composites, 2017.

[36] Batista NL, Olivier P, Bernhart G, Rezende MC, Botelho EC. Correlation between degree of crystallinity, morphology and mechanical properties of PPS/carbon fiber laminates. Materials Research 2016;19:195–201. https://doi.org/10.1590/1980-5373-MR-2015-0453.

[37] Sun H, Ren P, Fried JR. The COMPASS force field: parameterization and validation for phosphazenes. Computational and Theoretical Polymer Science 1998;8:229–46.

[38] Eyckens DJ, Stojcevski F, Hendlmeier A, Randall JD, Hayne DJ, Stanfield MK, et al. Carbon fibre surface chemistry and its role in fibre-to-matrix adhesion. J Mater Chem A Mater 2021;9:26528–72. https://doi.org/10.1039/d1ta07151c.

[39] Yan Y, Xu J, Zhu H, Xu Y, Wang M, Wang B, et al. Molecular dynamics simulation of the interface properties of continuous carbon fiber/ polyimide composites. Appl Surf Sci 2021;563. https://doi.org/10.1016/j.apsusc.2021.150370.

[40] Wang H, Jin K, Wang C, Guo X, Chen Z, Tao J. Effect of fiber surface functionalization on shear behavior at carbon fiber/epoxy interface through molecular dynamics analysis. Compos Part A Appl Sci Manuf 2019;126. https://doi.org/10.1016/j.compositesa.2019.105611.

[41] Jiao W, Zheng T, Liu W, Jiao W, Wang R. Molecular dynamics simulations of the effect of sizing agent on the interface property in carbon fiber reinforced vinyl ester

resin composite. Appl Surf Sci 2019;479:1192–9. https://doi.org/10.1016/j.apsusc.2019.02.157.

[42] Jiao W, Hou C, Zhang X, Liu W. Molecular dynamics simulation of the influence of sizing agent on the interfacial properties of sized carbon fiber/vinyl ester resin composite modified by self-migration method. Compos Interfaces 2021;28:445–59. https://doi.org/10.1080/09276440.2020.1788305.

[43] Liu Y, Ai K, Lu L. Polydopamine and its derivative materials: Synthesis and promising applications in energy, environmental, and biomedical fields. Chem Rev 2014;114:5057–115. https://doi.org/10.1021/cr400407a.

[44] Liebscher J, Mrówczyński R, Scheidt HA, Filip C, Haìdade ND, Turcu R, et al. Structure of polydopamine: A never-ending story? Langmuir 2013;29:10539–48. https://doi.org/10.1021/la4020288.

[45] Zhang W, Wang Z, Lv S, Zhan W, Bai G, Zhou A, et al. Molecular simulation of different structure dopamine-modified graphene oxide and its effects on thermal and mechanical properties of the epoxy resin system. Polymer (Guildf) 2021;212. https://doi.org/10.1016/j.polymer.2020.123120.

[46] Yang P, Sun Y, Li G, Yang X, Zuo X. Tailored rigid-flexible interphase of M40X composites via block copolymers: A combined method of experimental analysis and molecular dynamic simulation. Compos B Eng 2023;257. https://doi.org/10.1016/j.compositesb.2023.110674.

[47] Wang C, He X, Tong L, Peng Q, Wang R, Li Y, et al. Theoretical prediction and experimental verification of pulling carbon nanotubes from carbon fiber prepared by chemical grafting method. Compos Part A Appl Sci Manuf 2013;50:1–10. https://doi.org/10.1016/j.compositesa.2013.03.008.

[48] Wang H, Jin K, Tao J. Improving the interfacial shear strength of carbon fibre and epoxy via mechanical interlocking effect. Compos Sci Technol 2020;200. https://doi.org/10.1016/j.compscitech.2020.108423.

[49] Nardin M, Schultz J. Relationship between fibre-matrix adhesion and the interfacial shear strength in polymer-based composites. Compos Interfaces 1993;1:177–92. https://doi.org/10.1163/156855493x00068.

[50] Weibull W. A statistical distribution function of wide applicability. J Appl Mech 1951. https://hal.science/hal-03112318.

[51] Naito K, Tanaka Y, Yang JM, Kagawa Y. Tensile properties of ultrahigh strength PAN-based, ultrahigh modulus pitch-based and high ductility pitch-based carbon fibers. Carbon N Y 2008;46:189–95. https://doi.org/10.1016/j.carbon.2007.11.001.